Journal of Asian Earth Sciences 120 (2016) 1–16

Contents lists available at ScienceDirect

Journal of Asian Earth Sciences

journal homepage: www.elsevier.com/locate/jseaes

Timing and origin of migmatitic gneisses in south Karakoram: Insights from U–Pb, Hf and O isotopic record of zircons

Munazzam Ali Mahar [a,*], Gweltaz Mahéo [b], Philip C. Goodell [a], Terry L. Pavlis [a]

[a] Department of Geological Sciences, University of Texas at El Paso, El Paso, USA
[b] Université de Lyon, F-69622 Lyon, France Université Lyon 1, Villeurbanne ENS, Lyon CNRS, UMR 5276, Laboratoire de Geologie de Lyon, BAT Géode, 2 rue Dubois, 69622 Villeurvanne, France

ARTICLE INFO

Article history:
Received 16 October 2015
Received in revised form 14 January 2016
Accepted 18 January 2016
Available online 28 January 2016

Keywords:
India–Asia convergence zone
Migmatitic gneisses
Neogene partial melting
Proterozoic inherited core
Zircon dissolution

ABSTRACT

The timing and origin of partial melting in collision belts is crucial to understand the thermotectonic evolution and the relationship between HT metamorphism and magmatism in over-thickened crust. In the present study, we used the in-situ isotopic (Hf, O and U–Pb) record of zircons to investigate the timing and origin of migmatitic gneisses exposed in the core of the Dassu dome in south Karakoram. The new U–Pb zircon dating identified the Proterozoic inherited cores (1.8–1.9 Ga and 2.3–2.5 Ga) surrounded by a Neogene overgrowth with ages ranging from ~6 to ~20 Ma. These ages imply that the partial melting in the Karakoram Metamorphic Complex lasted from >20 Ma to ~6 Ma and can be correlated with the Miocene magmatism in the adjacent Baltoro region. Oxygen isotopic data from Proterozoic inherited cores (1.8–1.9 Ga) and Neogene overgrowths are indistinguishable and generally vary from 8‰ to 9.5‰. These values are slightly higher than the most igneous zircons (6.5–8‰, Valley et al., 2005) indicating an igneous precursor with heavy initial O composition that later might have equilibrated with low temperature environment or some involvement of supracrustal material is likely. However, a few low U/Th, relatively old inherited cores (2.3–2.5 Ga) showed mantle-like ($\delta^{18}O = 5.3 \pm 0.6$‰, Valley et al., 2005) values of $\delta^{18}O = 5.5 \pm 2.7$‰. The present-day weighted mean εHf (0) of the Proterozoic inherited cores ranges from -50 ± 1.0 to -44.3 ± 1.2. In contrast, the Neogene rims are 15–20 ε-units higher than the inherited core with present-day εHf (0) = -30.6 ± 0.9. This implies that the Hf composition of the Neogene overgrowth is not controlled exclusively by the dissolution of the inherited cores and that contamination by external melts is likely. We suggest a contribution from the Neogene, less-evolved magmatism in the Baltoro region (εHf (0) = ~−4 to −10). The elevated oxygen composition is not consistent with the contribution from pristine mantle-derived magmas. The observed homogeneous and uniform Hf–O isotopic composition of the Proterozoic inherited cores suggest their derivation from mildly evolved infracrustal sources with minor input from supracrustal material. The older inherited zircons (2.3–2.5 Ga) were precipitated from juvenile mantle derived magmas.

1. Introduction

Partial melting in the continental crust is one of the major features of convergent zones. In active collision zones, such as the Himalayas, crustal partial melting, as illustrated by the occurrence of many syn-collision migmatite outcrops, is well documented in the lower or underthrusting Indian plate (Le Fort, 1986; Le Fort et al., 1987; Harris and Massey, 1994; Guillot and Le Fort, 1995; Visona and Lombardo, 2002; Guo and Wilson, 2011 and references therein). Also, based on geophysical data, present-day partial melting of the underthrusting Indian plate beneath the southern Tibet until the Bangong–Nujiang Suture has been suggested (Nelson et al., 1996). However, within the Tibetan plateau partial melting of the upper plate (the Lhasa block, the southern part of the Asian plate) is not documented as no outcrops of migmatitic rocks produced after the India–Asia contact have been observed so far. In south Karakorum, the western prolongation of the Lhasa block, Neogene migmatites and granites have been recognized (Bertrand et al., 1988; Searle et al., 1989, 2010; Allen and Chamberlain, 1991; Lemennicier et al., 1996; Rolland et al., 2001) (Fig. 1). Therefore, south Karakoram provides the opportunity to study the deep crustal behavior, within the upper or overriding plate of the India–Asia convergent zone. However, the timing of partial melting and final crystallization related to the migmatite formation is not well established. Establishing the history of the

* Corresponding author.
E-mail address: mali3@miners.utep.edu (M.A. Mahar).

http://dx.doi.org/10.1016/j.jseaes.2016.01.014
1367-9120/

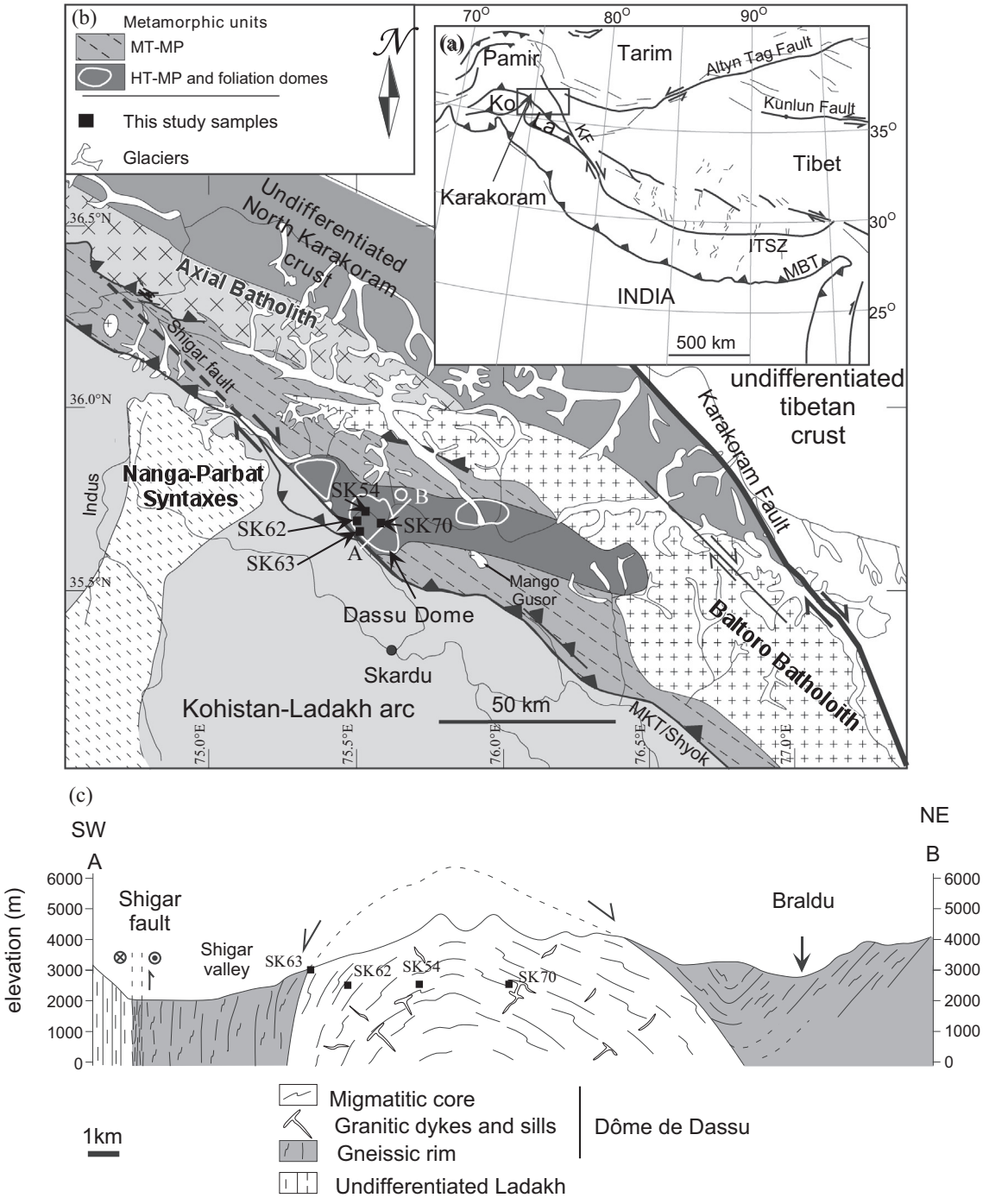

Fig. 1. (a) Location of the studied zone, (b) geological map and (c) geological cross section of the Dassu dome showing the sample location. MBT: Main Boundary Thrust, MKT: Main Karakoram Thrust, ITSZ: Indus Tsangpo Suture Zone, KF: Karakoram Fault, Ko: Kohistan, La: Ladakh, GC: Garam Chashma (after Mahéo et al., 2004; Pêcher et al., 2008).

migmatite formation would allow to reconstruct the thermal evolution of the upper plate and then to discuss its geodynamic evolution in the framework of the Himalaya–Tibet tectonic, petrologic and morphologic evolution.

This study focused on the Dassu dome, mid-crustal migmatitic gneisses exposed in the South Karakoram (Fig. 1). We measured the first in-situ U–Th/Pb age of zircon to reconstruct the timing of the partial melting and final crystallization. We also obtained in-situ O and Hf isotopic composition of the dated spots on inherited core and Neogene overgrowth to discuss the origin of the partial melts and test potential implication of mantle melts.

2. Geological setting

The Karakoram Range forms part of the south Asian continental margin, located to the west of and separated from southern Tibet by the Karakoram fault (KF, Fig. 1). Its southern boundary is the south verging Main Karakoram Thrust, an active structure (Searle et al., 1989; Pegler and Das, 1998; Seong et al., 2008) that was initially activated during the Cretaceous collision of the Kohistan–Ladakh arc with the South Karakoram active margin (Coward et al., 1986). The Kohistan–Ladakh arc formed in response to intra-oceanic subduction of Tethyan oceanic crust south of the

Karakoram during the Mid-Cretaceous (Coward et al., 1986). Around 50 Ma, the Kohistan–Ladakh arc was obducted onto the Indian margin along the Main Mantle Thrust (MMT: Tahirkheli and Jan, 1979), which is the western extension of the Indus–Tsangpo Suture Zone. South of the arc, the Nanga Parbat–Haramosh massif consists of Proterozoic Indian crust (e.g., Treloar and Rex, 1990) that underwent rapid exhumation associated with synchronous metamorphism and anatexis during ~12 Ma to 0.7 Ma (Zeitler, 1985; Butler and Prior, 1988; Butler et al., 2002; Zeitler et al., 2001; Crowley et al., 2009).

The Karakoram Range is divided into three domains from north to south (Fig. 1): (1) the North Karakoram terrane (e.g., Zanchi and Gaetani, 1994); (2) the Cretaceous–Miocene Karakoram axial batholith (Le Fort et al., 1983; Debon et al., 1987; Parrish and Tirrul, 1989); and (3) the Karakoram Metamorphic Complex, comprising Precambrian basement and a NW-trending metamorphic belt attributed to collision of the Karakoram block with the Ladakh–Kohistan arc and the Indian plate (Searle and Tirrul, 1991; Fraser et al., 2001). The initial collision coincided with an early, Barrovian metamorphic event (M1 = 0.7–1.2 GPa and 650–760 °C; Hanson, 1989; Lemennicier et al., 1996; Rolland et al., 2001, 2005; Searle et al., 2010; Palin et al., 2012) that ended with the emplacement of the 26.4 Ma Mango Gussar leucogranite (Fraser et al., 2001). Isograds for M1 are parallel to the major NW–SE striking regional foliation (Rolland et al., 2001). The M1 event is followed by the emplacement of the Baltoro granite and associated lamprophyric dykes between 25 and 13 Ma (Parrish and Tirrul, 1989; Schärer et al., 1990; Searle et al., 2010; Mahar et al., 2014). The Baltoro magmatic event is either related to a slab breakoff event (Rolland et al., 2001; Mahéo et al., 2002, 2009; Mahar et al., 2014) or thermal re-equilibration of thickened crust and extra heat derived from the mantle wedge (Searle et al., 2010). Lastly, a thermal event is associated with the migmatization and late granitic dyke emplacement (Fig. 1, M2 of Rolland et al., 2001; M4 of Searle et al., 2010; Palin et al., 2012). Migmatite formed a WNW–ESE-trending band of foliation domes (Fig. 1; Allen and Chamberlain, 1991; Lemennicier et al., 1996; Rolland et al., 2001; Searle et al., 2010) that crosscut the M1 structures (Rolland et al., 2001). The cores of the domes represent rapidly exhumed high temperature (HT)-medium pressure (MP) diatexite and metatexite migmatites (Fig. 2; following the terminology of Sawyer, 2008), surrounded by amphibolite facies, sillimanite-grade gneisses (Rolland et al., 2001). Leucosome comprises 10–45% of the rock at the outcrop-scale (Mahéo et al., 2004). In detail, two zones have been distinguished: (1) a transition zone characterized by M1 relics (Kyanite + Staurolite + Muscovite + Garnet) overprinted by an M2 assemblage (Biotite + Sillimanite + Garnet); and (2) a high-grade zone with no apparent relics of M1 (Rolland et al., 2001). The M2 assemblage (~0.5–0.9 GPa and 650–770 °C) consists of migmatites and lower-granulite facies rocks (Fig. 2, Biotite + Sillimanite + K-feldspar + Garnet) (Rolland et al., 2001). So far, migmatization ages have been estimated at about 5–6 Ma (Smith, 1993; Fraser et al., 2001; Searle et al., 2010), based on monazite U–Th–Pb ages. These ages most probably represent the end of partial melt crystallization as monazite is dissolved in the migmatitic melts and forms during cooling just above the solidus temperature (Kelsey et al., 2008). However, (Rolland et al. (2006) reported amphibole Ar–Ar ages in the domes area, range from 19 to 9 Ma. This suggests that the HT event (M2) in the south Karakoram initiated earlier at c. 20 Ma at the time of intrusion of Baltoro granites (Mahar et al., 2014).

Lemennicier et al. (1996) concluded that contractional tectonics was in part, responsible for exhumation of the Karakoram gneiss domes. Rolland et al. (2005) proposed that the south Karakoram domes are located at the axial domain of crustal-scale folds and their formation is related to the diapyric amplification of the folds. Although contraction could explain the deformation pattern observed in the gneisses surrounding the migmatitic cores. Mahéo et al. (2004) argued that shortening could not account for the HT-deformation of the migmatitic cores which appear dominated by normal-sense structures and a radial displacement strain field. This observation is consistent with a buoyancy-driven diapiric ascent (i.e., Teyssier and Whitney, 2002) as a possible mechanism for dome formation in Karakoram. Additional mechanisms are required to facilitate low temperature (LT) exhumation. Allen

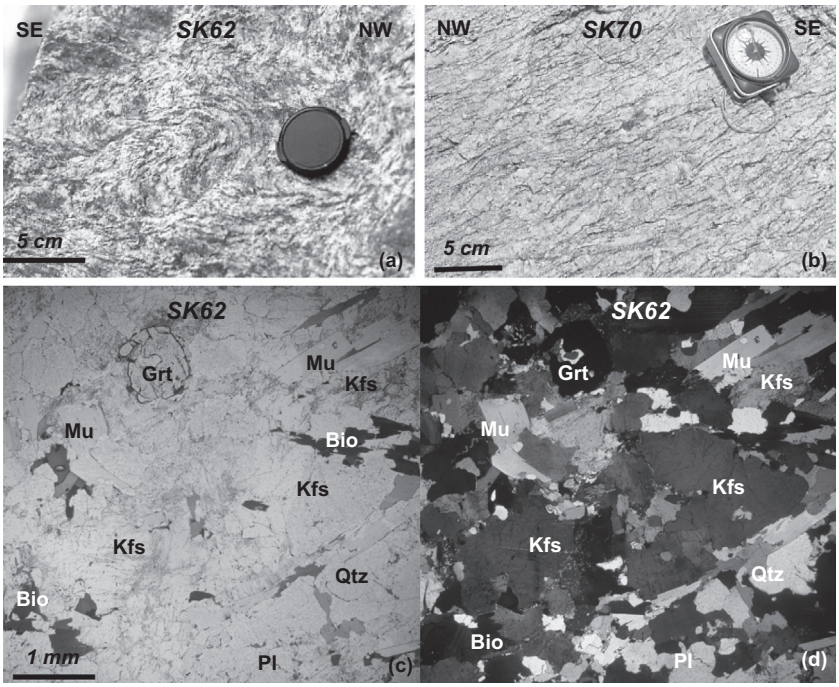

Fig. 2. Petrographic characteristic of the studied sample. Field photography of samples SK62 (a) and SK70 (b) migmatites, and photomicrograph of sample SK62 leucosome area in plane polarized light (c) and cross polarized light (d). Bio: biotite, Grt: Garnet, Kfs: K-feldspar, Mu: Muscovite, Pl: plagioclase and Qtz: quartz.

and Chamberlain (1991) and Mahéo et al. (2004) proposed a two-stage model: (1) HT-exhumation by syn-contractional diapiric ascent of partially molten middle crust followed by (2) late-stage LT-exhumation due to exhumation and erosion during crustal-scale folding. The cross-cutting feature of the isograds around the panmah dome (20 km east of Dassu dome; see Fig. 1) for instance, argues for the crustal scale fold for being slightly older than the dome. This indicates that a significant part of the exhumation may also be related to the M1 evolution (Rolland et al., 2005). The extension in the upper crust (i.e., pull apart) could be an alternative mechanism for dome emplacement as explained by Rey et al. (2009a,b, 2011). However, pull-apart type structures fail to be observed in the study area. The domes lineament is found in the core of a structure which is not directly controlled by the strike-slip faults, but likely a E–W trending crustal scale fold.

3. Sample description

Zircons were extracted from four samples of migmatitic gneisses exposed in the Dassu dome in the western part of the Karakoram Metamorphic Complex (Fig. 1). Sample SK62 (35.68°N, 75.49°E, 2440 m) and SK63 (35.66°N, 75.50°E, 2480 m) were collected from the western part of the core and sample SK54 (35.72°N, 75.50°E, 2500 m) and SK70 (35.69°N, 75.57°E, 2640 m) were collected from the eastern part of the dome (for location see Fig. 1). All samples belong to the High Grade Zone defined by Rolland et al. (2001) and are characterized by a discontinuous Biotite–Sillimanite migmatitic foliation (Fig. 2). Leucosomes are rich in K-feldspar; rare migmatitic garnets (produced as the peritectic product) have also been observed (Fig. 2).

4. Methodology

4.1. Design for zircon isotopic analyses

Zircons were separated by clean crushing, heavy liquid and magnetic separation techniques at The University of Texas at El Paso Mineral Separation Facility. Following separation, grains were handpicked, mounted in epoxy, and polished to expose crystal centers. Zircon texture description follows the nomenclatures presented by Corfu et al. (2003) and Hoskin and Black (2000). As far as possible, oxygen, U–Pb and Hf analyses were performed on the same spot or at least from the same growth domain. However, in some cases Hf analyses were not possible due to larger beam size (40 μm). The U–Pb and Lu–Hf isotopic analyses were done by multicollector laser ablation–inductively coupled plasma–mass spectrometry (LA–ICP–MS) at the Arizona LaserChron Center at the University of Arizona. The zircon U–Pb geochronology was done following method described in Gehrels et al. (2008, 2009) and Gehrels and Pecha (2014), while Hf isotopic measurements were performed using method described in Cecil et al. (2011) and Gehrels and Pecha (2014). The oxygen isotope measurements were carried out at WiscSIMS facility, University of Wisconsin using CAMECA IMS-1280 SIMS. The followed analytical method is fully described by Kita et al. (2009) and Valley and Kita (2009). Details of the methods are made available in supplementary material file "Analytical Methods". Oxygen analyses were performed first followed by U–Pb and Hf isotopic measurements.

Before analysis, zircons were imaged by Cathodoluminescence (CL) at the LaserChron SEM lab facility. Cathodoluminescence imaging is critical to identify internal domains within the grains, grain cracks, mineral inclusions and two-dimensional growth and recrystallization textures to guide spot placement onto least-disturbed growth domains.

5. Results

All the zircon isotopic data are presented in supplementary data tables. U–Pb and Hf data are listed in supplementary data Tables S1 and S2 respectively. Summarized oxygen data are listed in Table S3 while S4 shows the oxygen data along with standards and other analytical parameters. Summary of the isotopic data, presenting upper intercept ages and Hf–O isotopic record for the individual sample is made available in Table 1. Fig. 3 shows CL images of the analyzed zircons with labeled isotopic data. All uncertainties in supplementary U–Pb data table (S1) are reported at the 1-sigma level, and include only measurement errors. Systematic errors are as follows (at 2-sigma level): [1.5% ($^{206}Pb/^{238}U$) & 0.8% ($^{206}Pb/^{207}Pb$)].

5.1. Extracted zircon description

5.1.1. SK54

The CL images of zircons from sample SK54 reveal that almost all the grains are subhedral (Fig. 3). Zircons show obliterated oscillatory zoning; sector zoning was also observed in some grains. Local convolute zoning may be the result of recrystallization. Cathodoluminescence images revealed that the core of the grains in most cases is bright, homogeneous and rounded, while rims are usually darker. Zircon cores also show a few embayed structures, which may be the result of dissolution. The width to length ratio is 1:3 to 1:4 and size of the grains ranges from 200 to 400 μm in length.

Table 1
Summary of isotopic data.

Sample	Zircon zone	Age (Ma)	εHf (t)	εHf (0)	$\delta^{18}O$ (‰, VSMOW)
SK62	Core	1890 ± 20 (1)	−5.3 ± 1.0	−47.2 ± 1.0	8.8 ± 1.6
		n = 12	(MSWD = 1.3, n = 9)	(MSWD = 0.9, n = 9)	(n = 22, 2SD)
SK62	Rim	5.9 – 20 (2)		−30.6 ± 0.9	9.0 ± 0.7
		n = 15		(MSWD = 1.5, n = 14)	(n = 17, 2SD)
SK54	Core	1871 ± 3.4 (1)	−4.8 ± 0.9	−46.5 ± 0.9	8.5 ± 1.8
		n = 25	(MSWD = 1.4, n = 15)	(MSWD = 1.3, n = 15)	(n = 28, 2SD)
SK54	Rim	5.8 ± 0.2 & 10.0 ± 0.2 (2)		−47.5 & −46.5	8.3 & 8.2
SK70	Rim and core	1890 ± 6.2 (1)	−3.0 ± 1.3	−44.3 ± 1.2	8.4 ± 1.5
		n = 13	(MSWD = 1.9, n = 12)	(MSWD = 1.7, n = 12)	(n = 11,2SD)
SK63	Core	2243 ± 88 (1)	0.1–4.6	−50 ± 1.3	5.5 ± 2.7
		n = 4		(MSWD = 0.24, n = 4)	(n = 8, 2SD)
SK63	Rim and core	1836 ± 150 (1)	−7.1 ± 0.9	−47.1 ± 0.9	3.7 ± 2.5
		n = 6	(MSWD = 0.29, n = 7)	(MSWD = 0.37, n = 7)	(n = 7, 2SD)

(1) Upper intercept age, (2) concordant $^{206}Pb^*/^{238}U$ age. Weighted mean εHf values are at 95% confidence and mean $\delta^{18}O$ values shown with 2σ error. The εHf values correspond to the fractional deviation in parts per 10^4 from the contemporaneous value of a chondritic (Bulk Earth) reservoir with present-day $^{176}Hf/^{177}Hf$ = 0.282785 (Bouvier et al., 2008). MSWD: Mean Square of Weighted Deviates, VSMOW: Vienna Standard Mean Ocean Water.

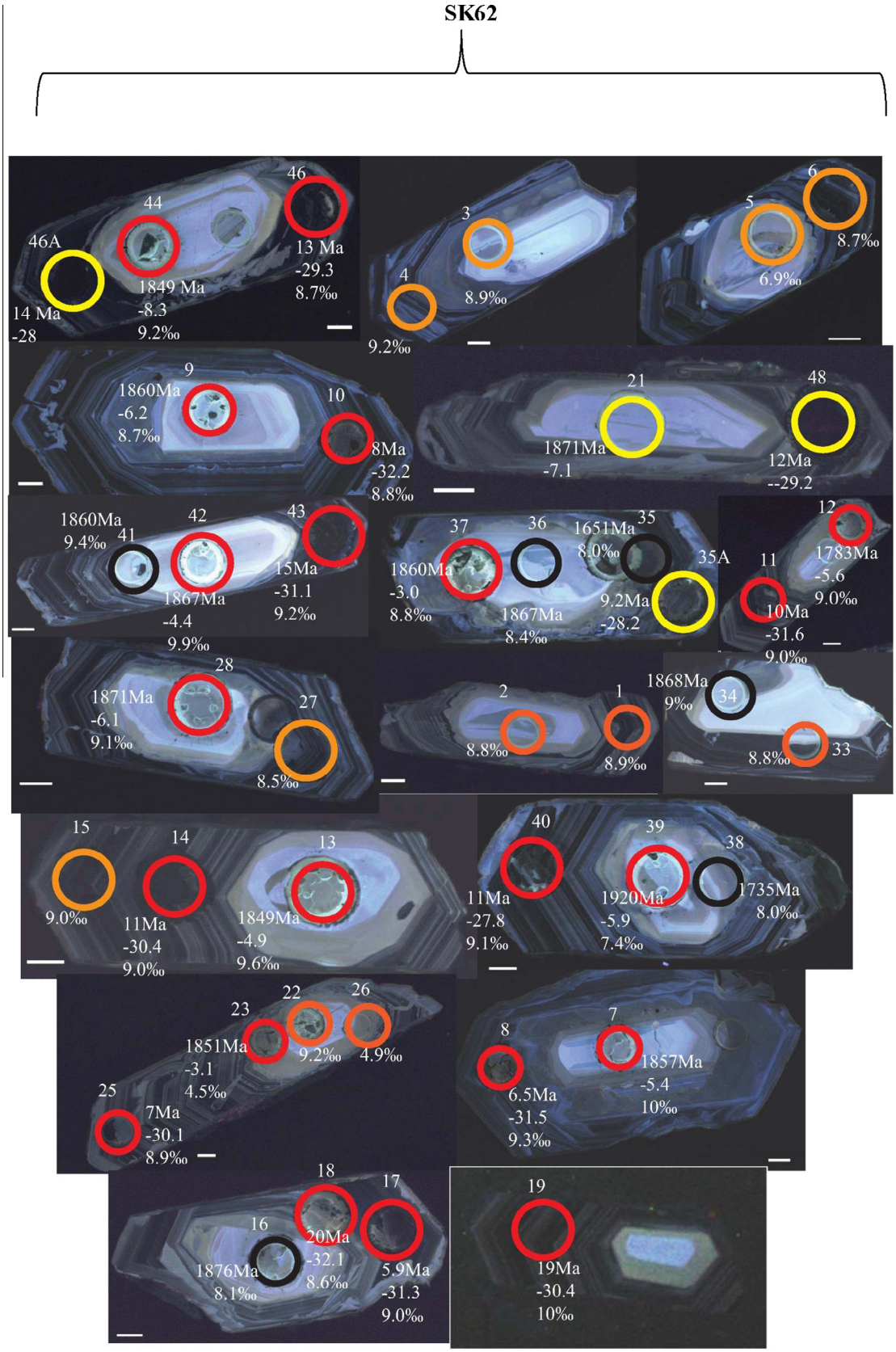

Fig. 3. Representative analyzed zircons and location of the analytical spots. Italic: spot number, *X* ‰: $\delta^{18}O$; *X* Ma: $^{206}Pb^*/^{207}Pb^*$ age; *X*: εHf (*t*). Red circles: spot with U–Pb, Hf and oxygen data, black small circles: spots with U–Pb and oxygen data, orange circle: oxygen only, yellow circle: U–Pb and Hf data. (For interpretation of the references to color in this figure legend, the reader is referred to the web version of this article.)

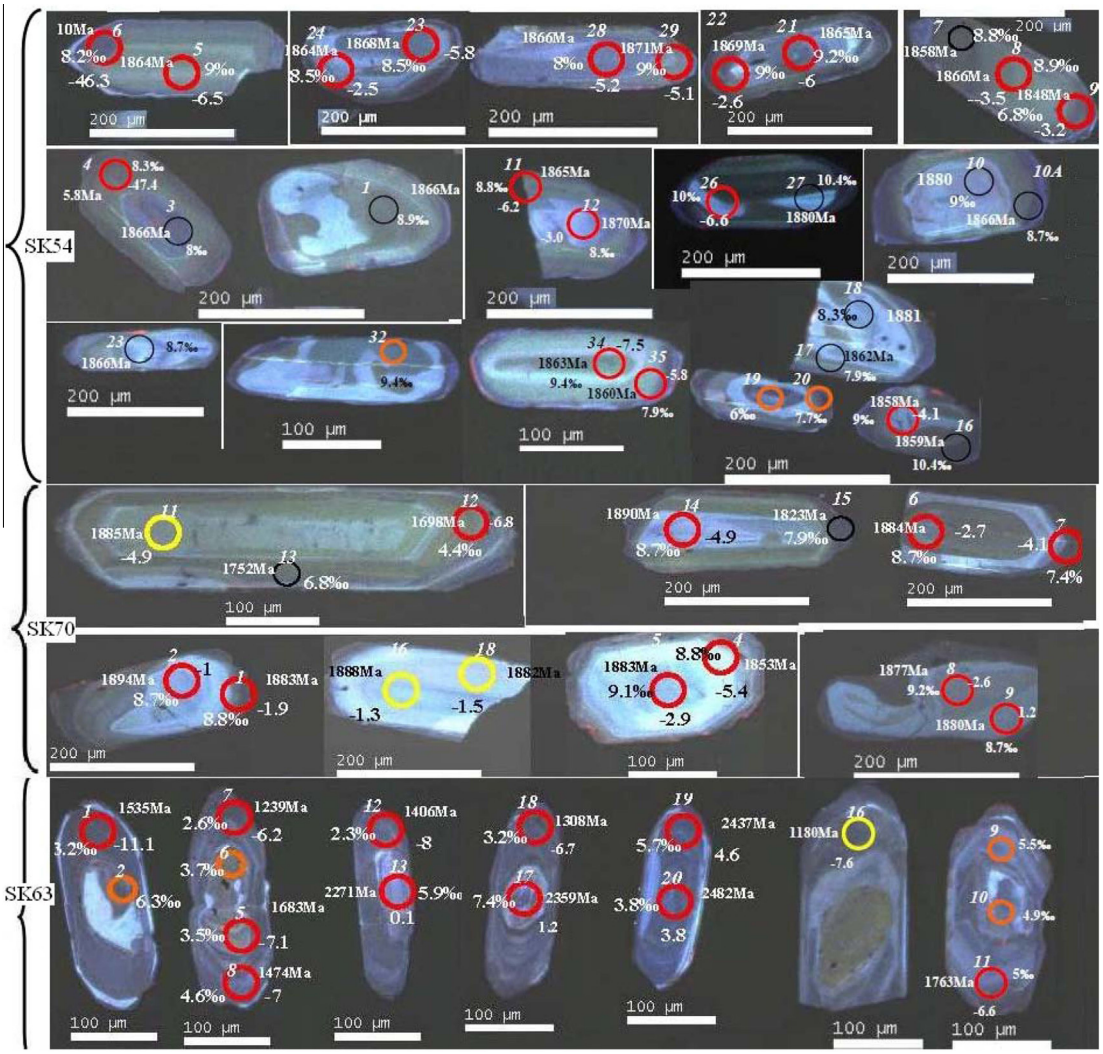

Fig. 3 (*continued*)

5.1.2. SK62

Zircons from this sample are mostly euhedral and prismatic with clear core-rim distinction (Fig. 3). Generally the core is homogeneous, very bright (high CL), euhedral to subhedral showing well-developed oscillatory zoning to partially obliterated primary growths. Cores are surrounded by dark colored (low CL) typical magmatic rims with strong oscillatory zoning. The width to length ratio is 1:3 and size of the zircon grains ranges from 200 to 400 µm in length.

5.1.3. SK70

In sample SK70, zircons are subhedral and cores are bright under CL with almost no visible zoning (Fig. 3). Some darker cores have also been observed. The core is surrounded by both low and high CL overgrowths. The outermost part of the grains is very thin, low CL overgrowth with irregular and altered zoning. The length to width ratio is 1:3 and size of the grains ranges from 200 to 400 µm in length.

5.1.4. SK63

Zircons from sample SK63 are subhedral and prismatic with clear core and rim distinction (Fig. 3). The core is generally subhedral to irregular with obliterated primary zoning. Rims present oscillatory zoning and are generally darker. Their rusty appearance as well as diffused obliterated zoning suggests a late alteration. The outermost part of the grains is a very thin bright overgrowth. The width to length ratio is 1:2 and size of the zircon grains ranges from 100 to 300 µm in length.

5.2. U–Pb geochronology

Many ages are discordant, and follow a discordia line that was used to calculate the upper and lower intercept ages (Fig. 4a–d). We also report the weighted mean (WM) age for the analyses with >90% concordance (Fig. 4e). In two samples Neogene overgrowth around Proterozoic inherited core is observed, these ages are shown as the Terra–Wasserburg plot (Fig. 4f)

5.2.1. SK62

A total of 32 analyses were carried out on 15 zircon grains from rim to core. The strongly zoned magmatic overgrowths that appeared dark in CL images are enriched in U. Majority of the rims have uranium content higher than 5800 ppm. Their U/Th ratio varies from 10 to 63. In contrast, Proterozoic inherited cores are generally very low in U (146–608 ppm). Three highly discordant (disc ~70%) analyses have U content >900 ppm.

All the inherited cores define a clear discordia line with a well-defined upper intercept age of 1890 ± 20 Ma and a poorly con-

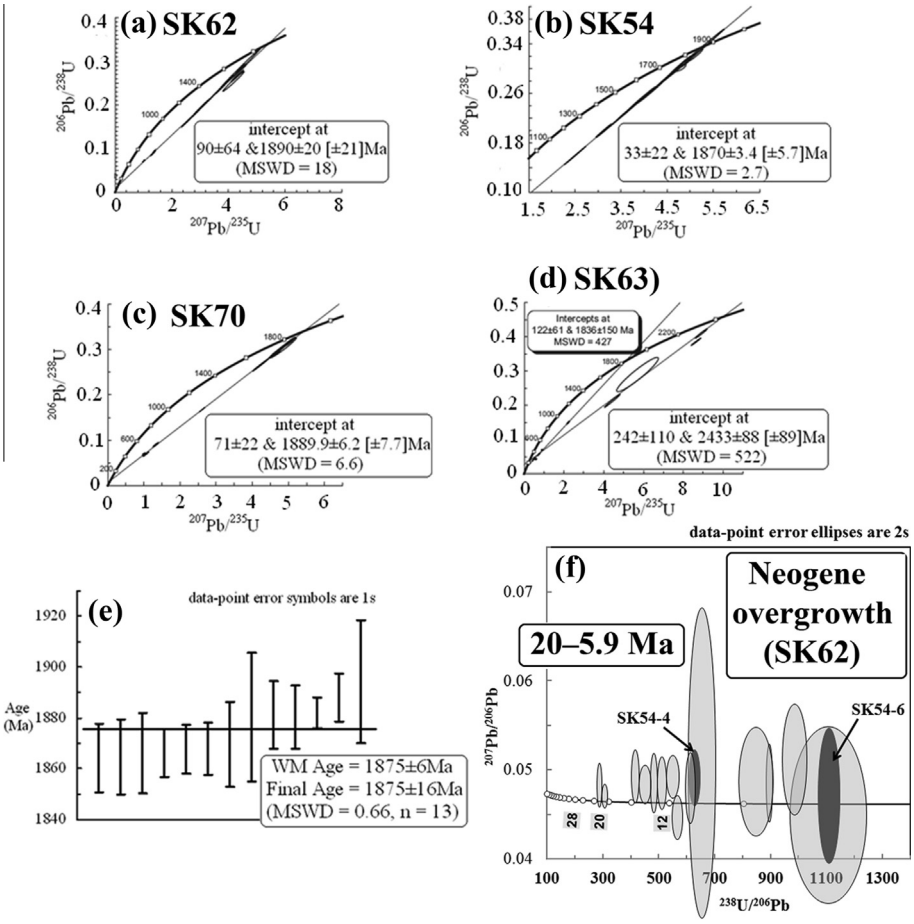

Fig. 4. Zircon U–Pb individual Concordia plots for studied samples. (a–d) Represents inherited Proterozoic cores. Note that sample SK63 zircons are highly discordant yielding a younger upper intercept age of 1836 ± 150 Ma (MSWD = 427). SK63 also recorded the oldest ages in the area of 2.27–2.48 Ga. (e) Weighted mean age of inherited core based on the analyses with <10% discordance, (f) Terra–Wasserburg plot of Neogene overgrowth.

strained lower intercept at 90 ± 64 Ma (Fig. 4a). Two greenish outer cores, SK62-23and 38 showed extreme discordance (>65%).

Analyses (n = 15) on rims yielded ages ranging from 5.9 to 20 Ma (Fig. 4f). The youngest of these ages is consistent with the previously reported migmatite ages based on U–Pb monazite dating (Fraser et al., 2001; Searle et al., 2010).

5.2.2. SK54

A total of 27 analyses were carried out on 14 grains. Most analyses yielded discordant ages, defining a clear discordia line with an upper intercept age of 1870.6 ± 3.4 Ma (Fig. 4b). Two analyses on rims yielded concordant ages of 5.8 ± 0.2 Ma and 10 ± 0.2 Ma (shown as dark gray ellipses in Fig. 4f). The inherited cores are deficient in U and Th. Uranium concentration ranges from 71 to 665 ppm with one sample above 1000 ppm and U/Th ratio of cores vary from 0.7 to 9.3 with one outlier of above 10. The lower U/Th ratio suggests that the inherited cores are magmatic.

5.2.3. SK70

SK70 represents the Dassu migmatitic gneiss exposed at the eastern part of the dome just east of the Braldu River (Fig. 1). A total of 13 U–Pb analyses were carried out on seven zircon grains. All analyses are discordant and define a discordia line with an upper intercept of 1889.9 ± 6.2 Ma (Fig. 4c). Similarly to the other two migmatite samples, the U concentration ranges from 118 to 610 ppm with two samples above 900 ppm and U/Th varies from 1.6 to 10.9 with three analyses above 15. No Neogene ages were identified in this sample.

5.2.4. SK63

A total of 11 analyses were carried out on seven zircons. Four points (old inherited cores) yielded very old $^{206}Pb^*/^{207}Pb^*$ ages, ranging from 2.3 to 2.5 Ga. In addition, seven highly discordant ages define a discordia line similar with the ones defined by the previous samples (upper intercept at 1836 ± 150 Ma and lower intercept at 122 ± 61 Ma) (Fig. 4d). The cores are lower in U (165–244 ppm) with corresponding U/Th ratio ranges from 1.4 to 12.4. While the rims are enriched in U (804–1537 ppm) and corresponding U/Th ranges from 20.1 to 31.5 with one outlier of 1.8. No Neogene overgrowth has been measured.

5.3. Inherited weighted mean age for the Dassu migmatitic gneisses

Data with concordance >90% (13 points, four from SK70 and nine from SK54) yielded a mean $^{206}Pb^*/^{207}Pb^*$ age of 1875 ± 16 Ma (Fig. 4e). Therefore, it may be inferred that the major contribution is from the 1870–1890 Ma-old source. However, there may be a minor contribution from an older source (2.3–2.5 Ga), which is only observed in sample SK63.

5.4. Zircon Hf isotope data

Initial weighted mean (WM) εHf (t) values were calculated at upper intercept ages. The Hf isotopic data in terms of WM initial εHf (t) and projected present-day εHf (0) shown in Fig. 5 are at 95% confidence interval. The present-day εHf (0) for the inherited

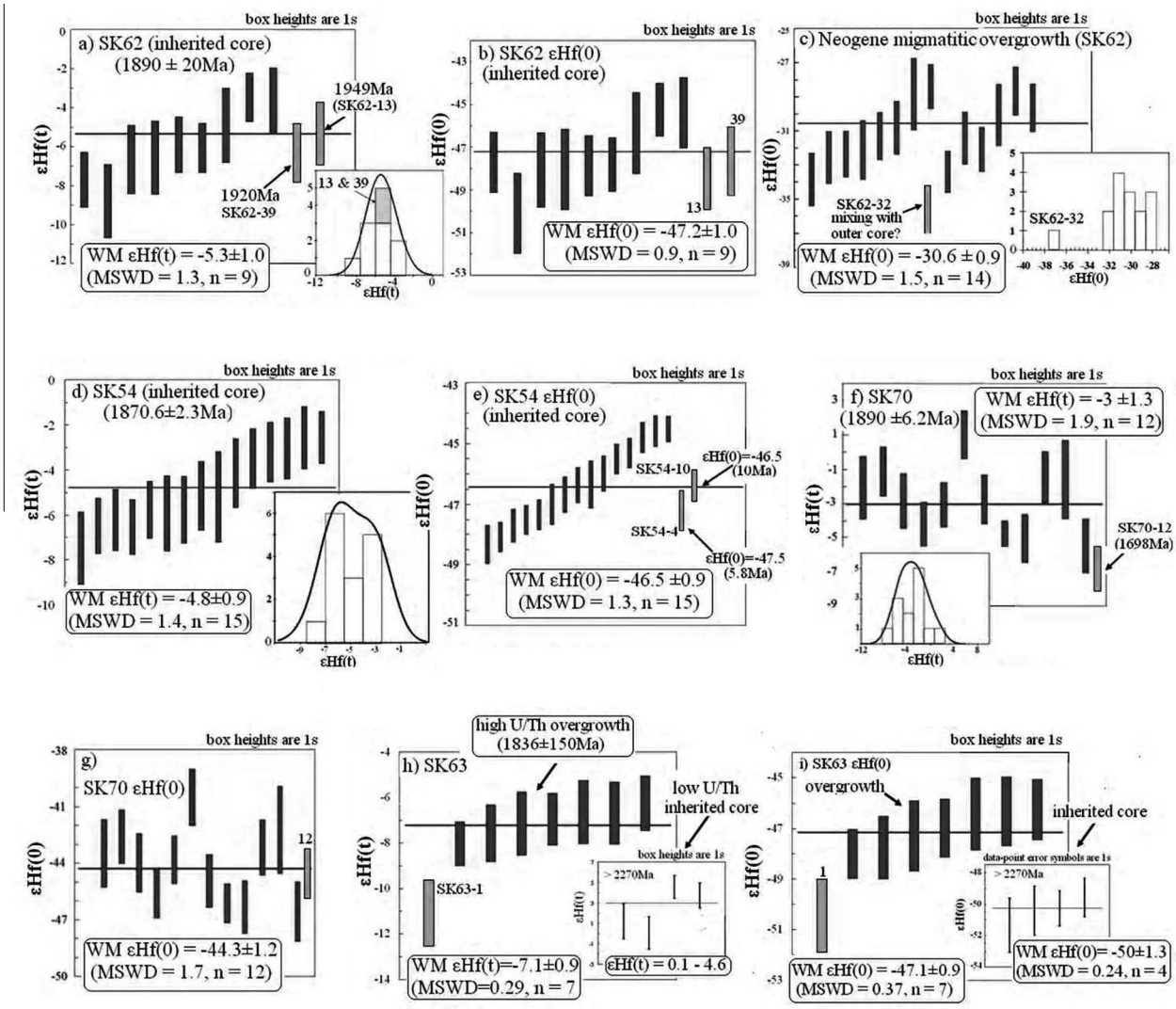

Fig. 5. Hf isotopic compositions in terms of initial εHf (*t*) and present-day εHf (0) (at 95% confidence interval) of the studied zircons.

core is calculated to compare with the Hf composition of Neogene overgrowth.

5.4.1. SK62

A total of 27 analyses were performed on 14 selected zircon grains, 12 analyses were carried out on inherited cores while 15 analyses (12 zircons) were carried out on Neogene rims. The calculated weighted mean initial εHf (*t*) of the inherited zircons at 1890 Ma is −5.3 ± 1.0 (MSWD = 1.3, *n* = 9), ranging from −8.3 to −3.1 with a scatter of 5.2 ε-units (Fig. 5a). The present-day WM εHf (0) is −47.2 ± 1.0 (MSWD = 0.9, *n* = 9) ranging from −50.1 to −45.4 with a scatter of 4.7 ε-units (Fig. 5b). Two older cores with ages >1920 Ma (SK62-13 and SK62-39) that do not fall on discordia line are not included in the WM calculations. However, the Hf isotopic composition of these two older cores is indistinguishable from 1890 Ma population.

Given the very young ages of Neogene overgrowth (20–5.9 Ma), very little decay has occurred since the time of crystallization. We report here only the present-day Hf isotope composition for these younger overgrowths. The WM εHf (0) for the Neogene overgrowth is −30.6 ± 0.9 (MSWD = 1.5, *n* = 14) ranging from −28.0 to −33.0 with a scatter of 5 ε-units except one rim (SK62-32) that shows a lower value of −37.1 ± 1.7 (Fig. 5c). This highly non-radiogenic value may have resulted from later alteration processes and is therefore not included in WM calculations.

5.4.2. SK54

A total of 17 Hf analyses were performed on 10 zircon grains. The Proterozoic inherited core (1870.6 ± 3.4 Ma) yielded a WM εHf (*t*) value of −4.8 ± 0.9 (MSWD = 1.4, *n* = 15) ranging from −7.5 to −2.5 with a scatter of 5 ε-units (Fig. 5d). The present-day WM εHf (0) for these zircons is −46.5 ± 0.9 (MSWD = 1.3, *n* = 15) (Fig. 5e). Two analyses on the Neogene rims SK54-4 (5.8 Ma) and SK54-6 (10 Ma) yielded the present-day εHf (0) of −47.5 and −46.5, respectively (which is identical and indistinguishable from the inherited core composition (Fig. 5e).

5.4.3. SK70

A total of 13 analyses were carried out on seven selected zircon grains (Fig. 3). The Proterozoic zircons (intercept age of 1889.9 ± 6.2 Ma) yielded a WM εHf (*t*) value of −3.0 ± 1.3 (MSWD = 1.9, *n* = 12) ranging from −5.5 to 1.2 with a scatter of 6.6 ε-units (Fig. 5f). Present-day WM εHf (0) is −44.3 ± 1.2 (MSWD = 1.7, *n* = 12) ranges from −46.6 to −40.5 with a total scatter of 6.1 ε-units (Fig. 5g). One younger (SK70-12, 1698 Ma, discordant) analysis does not fall on discordia line and is not included in

WM εHf (*t*) calculations. The εHf (*t*) for this younger zircon is −6.8 that is lower than the main zircon population while the present-day εHf (0) is −44.6.

5.4.4. SK63

A total of 12 zircon spots were analyzed on seven selected zircons (Fig. 3). Four analyses were carried out on older inherited cores; lower U/Th ratio and oscillatory zoning support their magmatic origin (~2.3 to ~2.5 Ga). Eight analyses were carried out on high U/Th, relatively younger (~1.2–1.8 Ga) overgrowths. This initial εHf (*t*) for the latter ranges from +0.1 to +4.6 (Fig. 5h, calculated on the individual ages). Their present-day WM εHf (0) is −50.3 ± 1.3 (MSWD = 0.24, *n* = 4) (Fig. 5i).

The high U/Th overgrowths with strongly discordant variable ages (1180–1763 Ma) defining an upper intercept age of 1836 ± 150 Ma yielded a WM εHf (1836 Ma) of −7.1 ± 0.9 (Fig. 5h, MSWD = 0.29, *n* = 7). The εHf (*t*) varies from −8.0 to −6.2 with a total scatter of 2 ε-units. The present-day weighted mean εHf (0) is −47.1 ± 0.90 (MSWD = 0.37, *n* = 7) (Fig. 5i).

One analysis SK63-1 showed a higher value of −11.3, which may result from analytical artifacts or overlapping with a thin veneer of the bright outer rim. This analysis is not included in the WM εHf calculation.

5.5. Oxygen isotopic data

5.5.1. SK62

Oxygen isotopic data for all inherited cores remain similar with a mean of $\delta^{18}O = 8.8 \pm 1.6‰$ (*n* = 22, 2σ) ranging from 6.9‰ to 10.2‰ with a spread of 3.3‰. The majority of analyses fall in the range of 8–9.6‰ (Fig. 6a). Two greenish outer cores (SK62-23 and SK62-26) yield highly discordant ages and show low $\delta^{18}O$ of 4.5 and 4.9‰, respectively. These values are regarded as altered zircons and were not included to calculate the mean $\delta^{18}O$ for the main zircon population. The Neogene rims (5.9–20 Ma) with perfect oscillatory zoning, share almost identical $\delta^{18}O$ values to their corresponding cores with a mean $\delta^{18}O = 9.0 \pm 0.7‰$ (*n* = 17, 2σ) ranging from 8.4‰ to 10.1‰ with a scatter of 1.7‰ (Fig. 6a).

5.5.2. SK54

The Mean $\delta^{18}O$ for the zircons of this sample is 8.5 ± 1.8‰ (*n* = 28, 2σ) ranging from 6.1‰ to 10.4‰ with a scatter of 4.3‰. The majority of the analyses fall in the range of 8–9.4‰ (Fig. 6b). Note that cores from this sample yielded almost identical oxygen composition to the SK62. Two Neogene rims (5.8 and 10 Ma) share similar isotopic values of $\delta^{18}O = 8.3$ and 8.2‰, respectively.

5.5.3. SK70

The sample yielded a mean $\delta^{18}O = 8.4 \pm 1.5‰$ (*n* = 11, 2σ) ranging from 6.8‰ to 9.2‰ (Fig. 6c). Eight analyses out of 12 yielded $\delta^{18}O = 8.7$ to 9.2‰. One greenish outer core with highly discordant younger age of 1698 ± 34 Ma showed the low $\delta^{18}O$ value of 4.4‰, which may be resulted by alteration and does not represent the main zircon population. Therefore, this analysis was not included in the mean $\delta^{18}O$ calculation.

5.5.4. SK63

A total of 15 analyses were carried out on six zircons. Eight analyses were carried out on inherited cores (2272–2482 Ma), while seven analyses were carried out on high U/Th younger rims

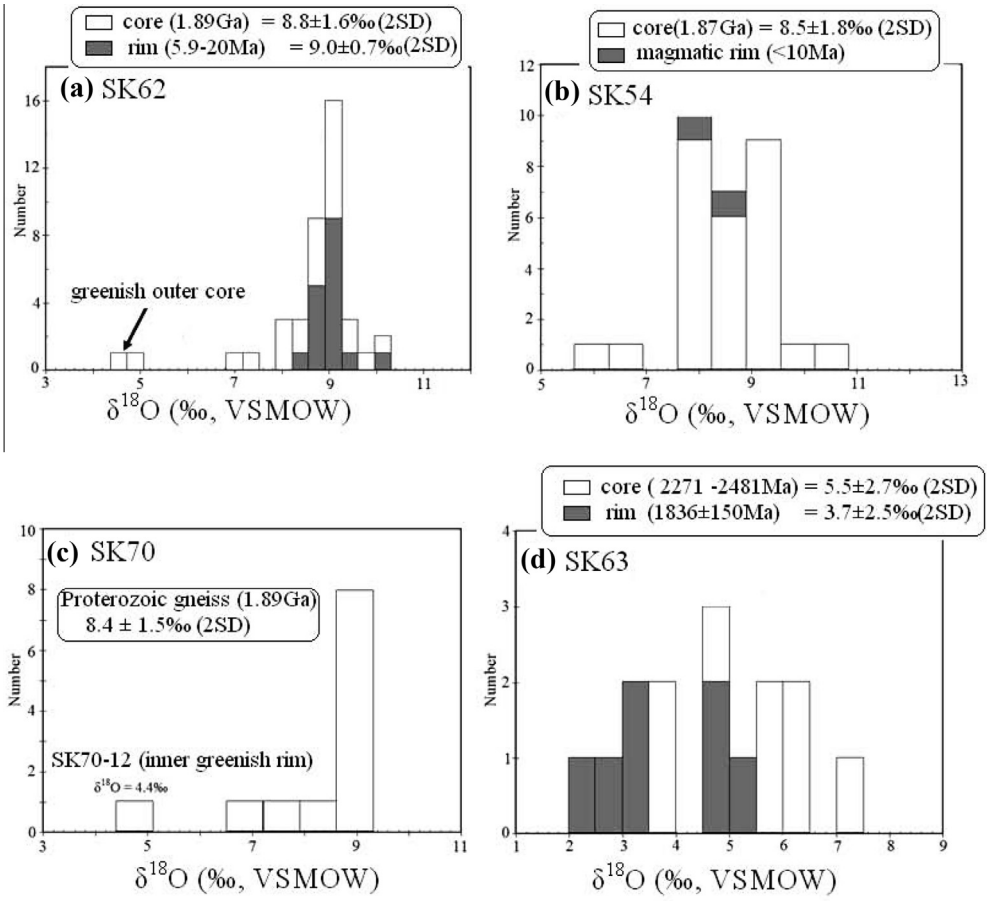

Fig. 6. Histogram of individual oxygen isotope analyses. Light color represents the older core and dark color represents the rims.

(1180–1763 Ma). The higher U/Th ratio of these rims suggest a metamorphic origin, however, the magmatic oscillatory zoning precludes further interpretation. The oldest inherited core yielded a mean $\delta^{18}O = 5.5 \pm 2.7‰$ ($n = 8$, 2σ), six samples fall in the range from 4.9‰ to 7.4‰ while two samples yielded very low $\delta^{18}O$ of 3.5 and 3.6‰. Seven analyses on younger metamorphic overgrowth yielded very low $\delta^{18}O$ with a mean $\delta^{18}O = 3.7 \pm 2.5‰$ ($n = 7$, 2σ) (Fig. 6d).

6. Discussion

6.1. Significance of inherited ages

Samples SK54, SK62 and SK70 present similar inherited ages defining clear discordia lines with upper intercepts at 1870.6 ± 2.3 Ma, 1890 ± 20 Ma and 1889 ± 20 Ma, respectively, and a poorly defined lower intercepts at 33 ± 22 Ma, 90 ± 64 Ma and 71 ± 22 Ma respectively. Data with concordance >90% (13 points, four from SK70 and nine from SK54) give a mean $^{206}Pb^*/^{207}Pb^*$ age of 1875 ± 16 Ma (Fig. 4). Inherited ages for SK63 are more complex. Altogether the inherited ages do not define a single discordia line, four points, from older inherited cores gave very old $^{206}Pb^*/^{207}Pb^*$ ages ranging from 2.3 to 2.5 Ga while the zircon rims show highly discordant ages (7 points) defining a discordia line similar to the ones defined by the previous samples (upper intercept at 1836 ± 150 Ma and lower intercept at 122 ± 61 Ma). Thus, our data suggest a major contribution from an 1870–1890 Ma old source as well as a minor contribution from an older source (2.3–2.5 Ga) only observed in sample SK63. All samples recorded thermal perturbation for which timing cannot be accurately defined. The 1.8–1.9 Ga event is known worldwide as the Transamazonian orogen (e.g. Zhao et al., 2002) and was also recognized in the south Lhasa block (Dong et al., 2011; Zhu et al., 2009, 2013). The 2.3–2.5 Ga ages have been obtained from core with irregular shape and sometime surrounded by younger overgrowth. This suggests that the oldest ages are detrital grains recycled during an earlier magmatic event. The younger overgrowths surrounding these oldest ages plot along the discordia line with upper intercept at about 1.8 Ga. Thus the oldest zircon core has most likely been recycled during the 1.8 Ga event.

The younger inherited zircon ages of ~1180 Ma and 500 Ma were also obtained from south Karakoram gneisses (Searle et al., 2010). Also, Ordovician sedimentary series (Le Fort et al., 1994; Rolland et al., 2002), overlying a Proterozoic meta-diorite crystalline basement with minimum Ar–Ar hornblende age of 651 Ma, thrusted by Cambro–Ordovician arc series (Rolland et al., 2002). That confirms that the south Karakoram is the western prolongation of the Lhasa terrane. All these characteristics as well as >2.3 Ga inherited ages have been recently interpreted as evidence that the Lhasa terrane originated from north of the Australian block before its northward drift at about 280 Ma (e.g. Zhu et al., 2013).

6.2. Origin of proterozoic inherited cores

Zircons in equilibrium with pristine mantle-derived melts have $\delta^{18}O$ value of 5.3 ± 0.3‰ with some slightly higher values (see Valley et al., 1998, 2005; Valley, 2003 for review). Overall, igneous zircon $\delta^{18}O$ values shift from 5.8 ± 0.74‰ during the Archean to 7.26 ± 1.55‰ during the Proterozoic. This shift is related to changes in the atmosphere, weathering, tectonics and crustal evolution (Valley et al., 2005). The only exceptions are zircons (higher $\delta^{18}O$ value of 13.5‰) from granitoids of Frontenac terrane (Shieh, 1985). However, almost 99% of reported $\delta^{18}O$ values from igneous zircons of any age are less than 10‰ with the predominant values falling in the range of 5–8‰. In contrast, sedimentary rocks have $\delta^{18}O$ value higher than 10‰ (see Valley et al., 2005 for review) and these heavy values are typically displayed in granitoids with a significant metasedimentary source.

The studied Proterozoic zircons from SK62, SK54 and SK70 (1.87–1.89 Ga) yielded homogeneous mean $\delta^{18}O$ values of 8.8 ± 1.6‰, 8.5 ± 1.8‰ and 8.4 ± 1.5‰ (at 2σ), respectively (Fig. 6a–c). The oxygen isotopic composition generally ranges from 7‰ to 9.5‰ (Fig. 7a). More than 90% zircons yielded $\delta^{18}O < 9.5‰$. These oxygen values are 1–2.5‰ higher than the typical igneous zircons in equilibrium with the high temperature environment. The low U/Th ratio and their observed oxygen values, 1–2.5‰ higher than the most igneous zircons (~7–8‰, Valley et al., 2005) suggest that the zircons were crystalized from the magma primarily generated by partial melting of pre-existing igneous protoliths with a minor contribution from a supracrustal (metasedimentary) component. The observed homogeneous oxygen composition indicates that the Proterozoic zircons crystallized from a magma source generated in a fairly closed system.

In contrast, the oldest, low U/Th inherited core from SK63 zircons (2.3–2.5 Ga) showed mantle-like values of $\delta^{18}O = 5.5 \pm 2.7‰$ ranging from 3.9‰ to 7.4‰ (Fig. 6d and a). This is in agreement with the Paleoproterozoic zircon oxygen composition from granitoids of other parts of the world (Valley et al., 2005). Zircons with $\delta^{18}O < 6.5‰$ are interpreted to be formed from the melt containing minor to negligible sedimentary component (Cavosie et al., 2005). However, the higher values, ~7.5‰ may result from interaction with surface water at low temperature, generating a slightly evolved magma from which zircons crystallized.

The discordant high U/Th rims of SK63 zircons, (poorly defining an upper intercept age of 1836 ± 150 Ma show very low and variable $\delta^{18}O$ values of 3.7 ± 2.5‰ (Figs. 6d and 7a). It is possible that the U–Pb system for these zircons was reset during a slightly younger thermal event and the melt was in equilibrium with low temperature crustal fluids/melts prior to recrystallization of zir-

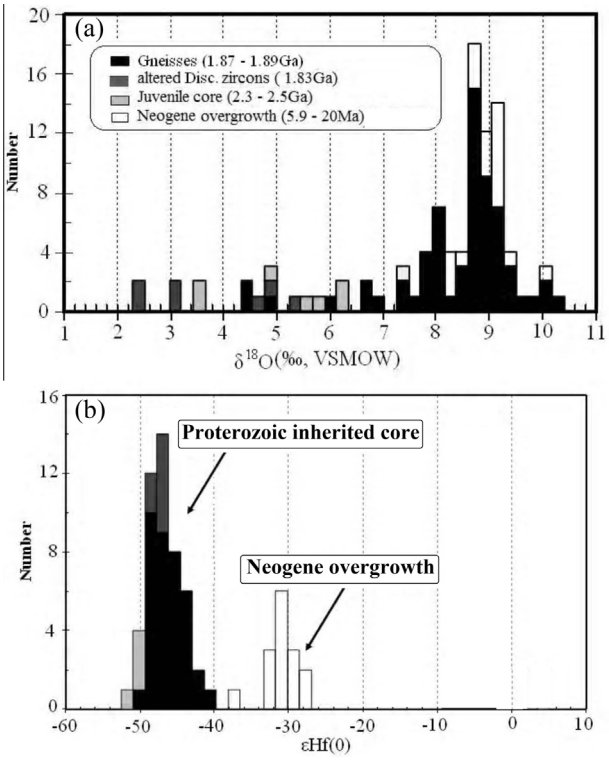

Fig. 7. $\delta^{18}O$ (a) and εHf (b) frequency histogram based on all the studied zircons, both initial and present-day except for Neogene overgrowth for which only present-day values are given.

cons. Alternatively, zircons could have been altered by sub-solidus processes interacting with low temperature fluids, resulting in low $\delta^{18}O$ values. The involvement of crustal fluids is also supported by their high U/Th ratio.

The overall variations in the present-day Hf isotope composition of inherited core and Neogene overgrowth are shown in Fig. 7b. The Neogene overgrowth is considerably less-evolved than the inherited zircons. One of the key observations is that none of these zircons approached the DM (Depleted Mantle) curve at the time of crystallization and stayed below the CHUR (Chondritic Uniform Reservoir) line (Fig. 8). Therefore the protolith for the (1.87–1.90 Ga) inherited cores cannot be juvenile and the magma from which zircons crystallized was derived by melting of preexisting crustal rocks, possibly infracrustal material with some supracrustal component, which is consistent with the oxygen isotopic record as well. SK63 low U/Th inherited cores yielded juvenile initial εHf (t) values ranging from +0.1 to +4.6 approaching the DM curve (Fig. 8a & b). Hf–O isotopic composition from these oldest zircons suggests that the zircons precipitated from the juvenile mantle-derived melts with minimal input from a supracrustal component. The high U/Th rims around these Paleoproterozoic juvenile magmatic cores yielded a WM εHf (t) of −7.1 ± 0.9 (Fig. 5d), and this is the most non-radiogenic signature, which again strengthens our interpretation that the SK63 highly discordant zircons possibly reset during a slightly younger thermal perturbation and interacted with crustal fluids/melt, or they crystallized from a magma with some sedimentary component.

The possible Hf evolution trend, projected as a line passing through the initial and present-day εHf values, cuts the DM curve at around 2.3–2.4 Ga indicating a crustal residence time of 400–500 Ma for the protolith (Fig. 8a). From this, it can be inferred that the igneous precursor may have separated from the mantle around 2.3–2.4 Ga (bold line, Fig. 8a) and has latter been recycled during the 1.8 Ga crustal melting event.

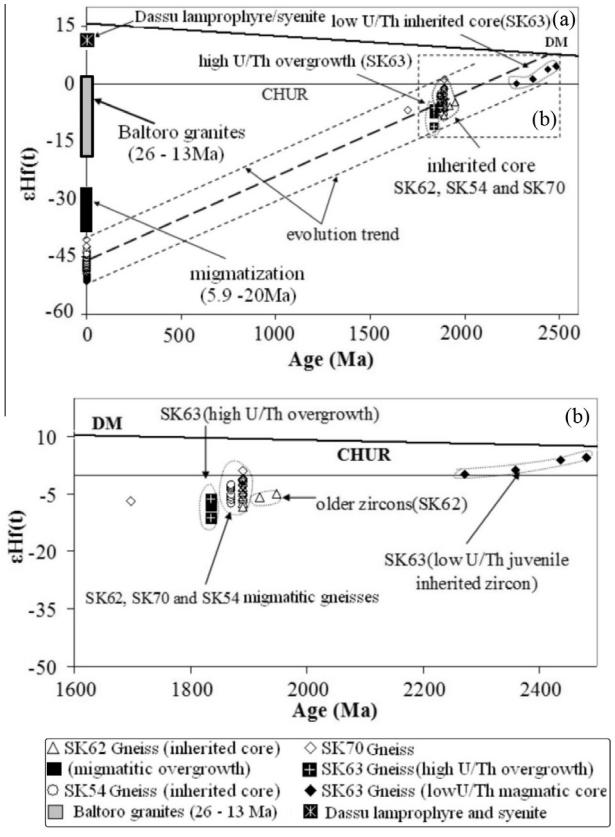

Fig. 8. Evolution of Hf isotopic composition with time and comparison with other south Karakoram magmatic rocks. Data points for lamprophyre, syenite and Baltoro granites are from Mahéo et al. (2009) and Mahar et al. (2014).

6.3. Timing of migmatite crystallization and partial melting

In partially melted metapelites, zircon overgrowth usually occurs during anatexis and specifically during melt cooling before final crystallization (Rubatto et al., 2013). Sub-solidus zircon growth is unlikely except for high pressure rocks which show zircon with patchy convolute zoning or lack of zoning (ibid.). Thus the Neogene overgrowths, associated with oscillatory zoning are most likely related with the migmatization.

The youngest ages obtained from zircon rims in samples SK62 and SK54, range from 5.8 to 20 Ma and all plot along the Concordia line in the Terra–Wasserburg plot with a tendency for the oldest ages (>12 Ma) to fall slightly above Concordia (Fig. 4f). For such young ages, it is difficult to distinguish discordance. Indeed, the observed age range might either reflect a discordia line with a lower intercept close to the minimum age (i.e. 5.8 Ma) or continuous zircon growth from 20 Ma to 5.8 Ma. This latter hypothesis is favored here as the older ages are always obtained from the inner part of the zircon rim and the younger are from the outermost part. Moreover, zircon composition (e.g., REE) changes with age (Fig. 9), which is best explained by progressive evolution of chemistry of the migmatitic melt. This evolution might be related to zircon growth as well as late crystallization of U-rich phases such as xenotime, uraninite or monazites. Previous monazite ages obtained from the Dassu migmatites (Smith, 1993; Fraser et al., 2001; Searle et al., 2010) are approximately ~5–6 Ma. As monazites mostly crystallized during cooling of migmatitic melts near to solidus temperatures (Kelsey et al., 2008), these monazite ages most likely represent the end of melt crystallization and coincide with the lower limit of our zircon U–Pb ages (Fraser et al., 2001; Searle et al., 2010). The crystallization ages from Neogene rims suggest that the partial melting of the Dassu migmatites initiated before 20 Ma (i.e. the oldest recorded age). Amphibole Ar/Ar ages from the amphibolite grade rocks surrounding the dome are as old as 17 Ma (Rolland et al., 2006) which suggests that the M2 event began significantly earlier than what is suggested by the monazite ages (i.e., ~5–6 Ma), which is also consistent with melting as early as 20 Ma. Another potential interpretation is that the age range is a mixing between two melting event, one older than 20 Ma and one at about 5–6 Ma. However there is no textural evidence for zircon resorption that would suggest multiple melting events. The oscillatory zoning is continuous and corresponding area usually gives a single age, except for widest grains. Moreover the evolution of the U content with age is not compatible with a mixing model (Fig. 9).

Continuous zircon crystallization from ~20 to 5–6 Ma implies relatively slow cooling. Based on the pressure-temperature evolution obtained on the Dassu dome by Rolland et al. (2001), zircon crystallization may have occurred below ~800 °C (M2 peak temperature) to 650 °C (temperature at which the PT path crosscut the metapelite solidus). From these data we obtain a cooling of about 120 °C between 20 Ma and 6 Ma, giving a cooling rate of 15 °C/Ma. This cooling rate is a mean value, and it is likely that cooling rate change during time. This is compatible with the South Karakoram cooling histories reconstructed from Ar/Ar dating and modeling, suggesting that a slow cooling event of about 10 °C/Ma occurred from 20 to 12–5 Ma (Schärer et al., 1990; Krol et al., 1996).

Zircon U–Pb data provide the timing of zircon crystallization. The relationship between zircon formation and partial melting has been modeled by Kelsey et al. (2008) and show that magmatic zircon crystallization took place during the melt cooling. Significant re-heating of the melt would induce zircon resorption and

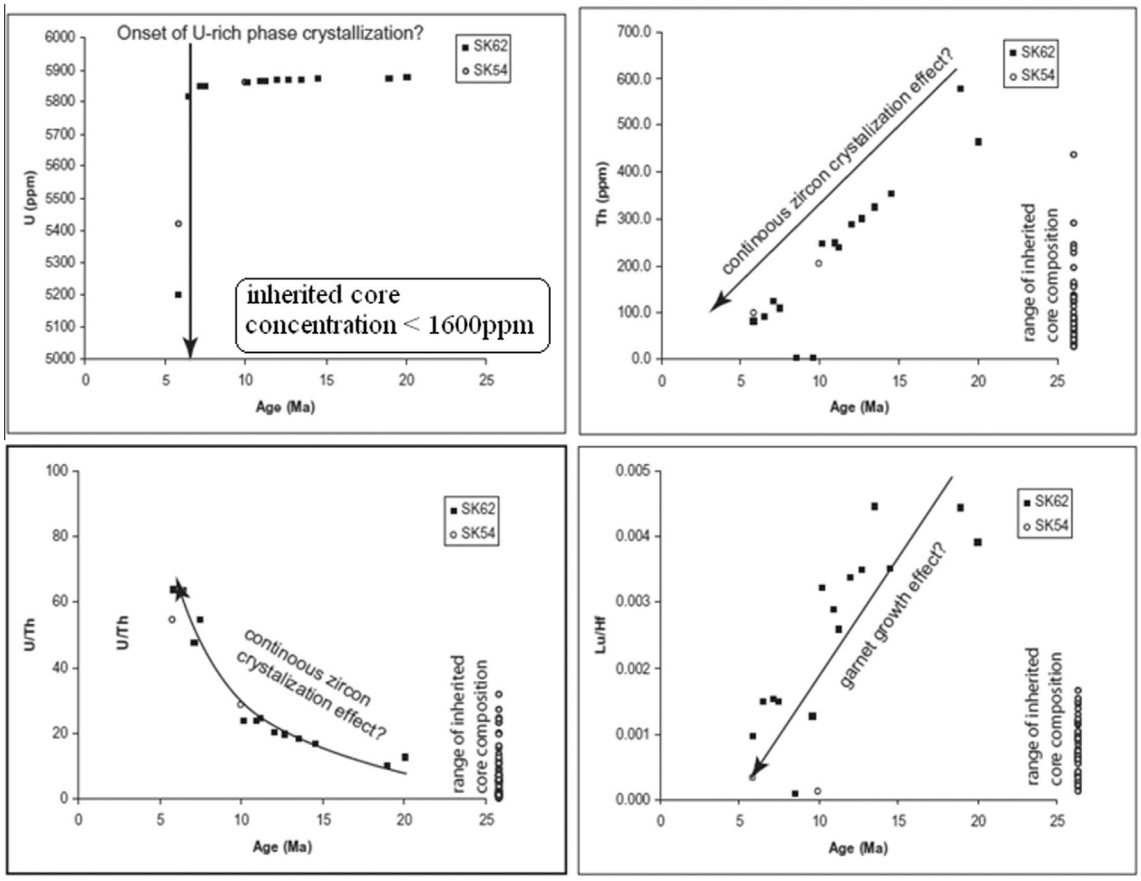

Fig. 9. Chemical evolution of Neogene overgrowth.

not a continuous oscillatory zoning as observed. Thus our zircon U–Pb data only allow us to constrain the timing of melt cooling, thereby only providing a lower bound for the onset of partial melting before 20 Ma. Note that this would still be true if the cooling is not monotonic or if the migmatitic melt was heated before final crystallization. Previous research shows that the migmatite formation took place after a main tectono-metamorphic event (M2–M3 of Searle et al., 2010; M1 of Rolland et al., 2001). The timing of this event is constrained by the emplacement of the Mango Gusar granite at 26.4 ± 1.3 Ma that crosscuts the metamorphic foliation (Fraser et al., 2001). Other crosscutting granites have been dated at ~25 Ma (Searle et al., 2010) and monazite and zircon from Karakoram gneisses gave U–Pb ages of 22–28 Ma (Searle et al., 2010; Palin et al., 2012). Thus, the timing of migmatization can be constrained between 20 Ma and 22 Ma, and the crystallization of early melt is contemporaneous with the Baltoro magmatic event (26–13 Ma, Searle et al., 2010).

6.4. Source of neogene migmatitic melt

One important question is what has melted and precipitated as magmatic rims during the Neogene thermal event? The Neogene overgrowths present $\delta^{18}O$ values (9.0 ± 0.7‰) indistinguishable, to the inherited cores as well as to the northward Baltoro granites (Mahar et al., 2014) (Fig. 10). Aside from a few zircons, none of the zircons fall in the mantle-like $\delta^{18}O$ range (Fig. 10). The remarkable similarities between the oxygen isotope composition of the overgrowths and the inherited cores is compelling evidence to infer that the Neogene overgrowth could be the precipitated melt generated by in-situ partial melting of Proterozoic mid-crustal host gneisses. The present-day Hf composition of Neogene overgrowth is also less variable with the weighted mean εHf (0) = −30.6 ± 0.9 suggesting in-situ melting. However, the Hf composition of Neogene rims is less-evolved than the inherited core (Figs. 9b, 10). The Neogene overgrowths are 15–20 ε-units more radiogenic than inherited cores. From the different, less-evolved Hf composition of overgrowth, it can be inferred that the Hf composition of the Neogene partial melt is not controlled solely by dissolution of zircons with composition similar to the inherited core. This indicates that the partial melting of the migmatite protolith alone would be insufficient to produce the εHf (0) structure observed in the

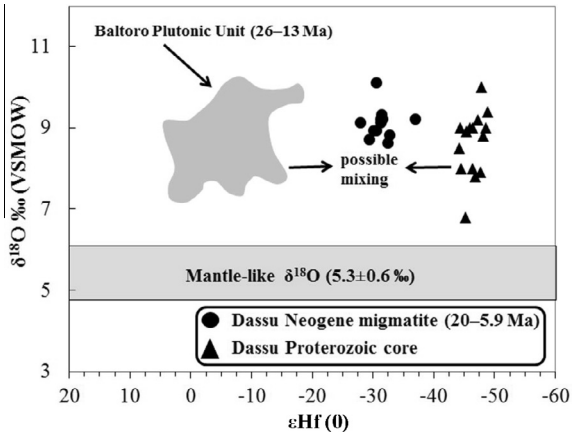

Fig. 10. Plot of εHf (0) vs oxygen isotope values. Mantle-like values are from Valley et al. (1998) and Valley et al. (2005). Gray field representing Hf–O isotope composition of Baltoro granites is from Mahar et al. (2014).

Neogene overgrowth. Generation of a more mafic character (as compared to the migmatite protolith) of the Neogene overgrowth could have several origins:

(1) Slight dissolution of radiogenic zircon in the magma can modify the Hf isotopic composition from being non-radiogenic to more radiogenic (Flowerdew et al., 2006). This hypothesis would require that other zircons than the one analyzed are present in the studied samples, which seems unlikely. The only sample with more juvenile zircons is SK63 with Paleoproterozoic inherited cores for which no evidence of dissolution is observed. This is supported by growth of highly non-radiogenic rims around these juvenile cores. SK63 juvenile cores only constitute a small fraction of the studied zircons, the majority of which present highly evolved present-day Hf composition. Moreover, no pronounced textural evidence (like corrosion, excavation and embayment) for zircon dissolution during melt generation is observed.
(2) An alternative possibility is the breakdown of minerals (excluding zircon) having a higher concentration of Lu; for example garnet, titanite, amphibole, pyroxene and other accessory minerals. The contribution from these minerals may significantly increase the $^{176}Hf/^{177}Hf$ ratio of the host magma. The metamorphic reactions for the HT metamorphism in the core of Dassu dome are fairly well constrained and the dominant partial melting reaction is biotite breakdown, Biotite + Sillimanite + Quartz ± Plagioclase = Garnet + K-feldspar + Melt (Rolland et al., 2001). Therefore, during the partial melting, instead of breaking down, garnet is crystallizing out of the magma as the peritectic product. Garnet breakdown may occur during decompression to form cordierite. However, no cordierite is reported from any microscopic studies from the Dassu core (Rolland et al., 2001) including our samples. Metamorphic studies reported no evidence of pyroxene or amphibole dissolution during migmatization at the peak temperature except in marbles/calc-schists (Rolland et al., 2001, 2005). Thus, the possible contribution from non-zircon minerals appears unlikely.
(3) Finally, there is the possibility of a contribution from a less-evolved melt. Contemporaneous south Karakoram magmatism includes both crustal (Baltoro) and mantle (lamprophyre and Hemasil syenite) melts. The whole rock hafnium isotope composition of these units (Mahéo et al., 2009) and zircon Hf isotopic values for the Baltoro granites (Mahar et al., 2014) are significantly higher than that measured in the Neogene overgrowth (Figs. 8a, 10), Baltoro granite: −10.4 to −1.8, Lamprophyre: −9.3 and Hemasil syenite: +10 to +12.2, (Mahar et al., 2014; Mahéo et al., 2009). Note that the zircon oxygen isotopic composition of Neogene overgrowth is indistinguishable from the Contemporaneous Baltoro magmatic rocks (Fig. 10). Consequently, contamination of the primary migmatitic (Proterozoic protolith partial melting) melt by any of these components might result in an increase of the εHf value relative to the inherited core composition. Thus, contamination seems likely; however, our data do not allow us to distinguish between crustal or mantle origin.

6.5. Origin of the South Karakoram neogene partial melting

In a continental convergent zone, crustal partial melting is usually associated with thermal re-equilibration of a previously thickened crust (Thompson and Connolly, 1995). In the south Karakoram, the M1 tectono-metamorphic event is most likely related to such a process and associated with emplacement of numerous granites (Searle and Tirrul, 1991; Rolland et al., 2001). The Neogene migmatite clearly appears as a distinct metamorphic event associated with a relatively high geothermal gradient (Rolland et al., 2001). The PT path of the Dassu migmatites implies high temperature and medium pressure conditions that are more likely explained by heat advection from intruded or underplated magmas than simple thermal re-equilibration of previously thickened crust (Rolland et al., 2001). Based on zircon U–Pb ages, Hf and O isotopic record of Dassu migmatite and Baltoro plutonic unit, a conceptual tectonic model is proposed (Fig. 11). As previously discussed that the partial melting that produced the migmatite is contemporaneous with the Baltoro granite emplacement. The Baltoro granites belong to a bimodal magmatic event including ultrapotassic, mantle related, magmas (shoshonite and lamprophyres, Rex et al., 1988; Pognante, 1991; Mahéo et al., 2002, 2009). Hence, the Baltoro granite as well as ultrapotassic melt emplacement may have provided the additional heat necessary for migmatization. This less-evolved Neogene magmatic event in south Karakoram has been related with break-off of the subducting Indian continental margin (Rolland et al., 2001; Mahéo et al., 2002, 2009) (Fig. 11).

6.6. End of partial melting event and late exhumation

Based on the earlier interpretations of the U–Pb monazite ages as well as our new U–Pb zircon data, it is inferred that the latest crystallization of the Dassu migmatites took place around 5 Ma. The end of melting implies cooling below the solidus temperature (~650–700 °C). Based on previously published P–T paths recorded by the Dassu migmatite such temperatures are reached for pressure of ~2–3 kbar (Rolland et al., 2001) as the peak temperature of ~800 °C was reached at ~5–6 kbar (Rolland et al., 2001; Searle et al., 2010). Thus, the end of partial melting is related to the migmatite exhumation. Assuming a minimum age of 20 Ma for the temperature peak at 5–6 kbar and 5 Ma for the cooling at solidus temperature at 2–3 kbar we obtained a mean exhumation rate of 0.5–1 mm/yr from 20 to 5 Ma and 1.5–2.2 mm/yr from 5 Ma to present time. This suggests that two exhumation events took place. Early, high temperature, exhumation is related, in part at least, with doming as evident from tilted way-up criteria, dykes and sills (Rolland et al., 2001). This doming has been related to South-Southwest – North-Northeast compressive deformation (Lemennicier et al., 1996; Searle and Tirrul, 1991) or vertical extrusion along the Main Karakoram Thrust (Lemennicier et al., 1996). Detailed structural analysis by Mahéo et al. (2004) showed evidence that high temperature deformation is dominated by radial extensional deformation. This radial extension was interpreted by Mahéo et al. (2004) as the product of high temperature diapiric motion (Fig. 11). However, this type of exhumation process is only efficient at high temperature and other mechanisms must be invoked to account for the exhumation of the Dassu migmatite to the surface. Mahéo et al. (2004) suggested that late exhumation was related with exhumation and erosion of south Karakoram accommodated by the MKT reactivation. Such exhumation might explain the transition from slow (before 5 Ma) to fast (after 5 Ma) exhumation. However, the timing of the MKT reactivation as well as the Pliocene exhumation history of south Karakoram needs to be estimated to properly constrain the recent exhumation history.

6.7. Implication for the behavior of the Asian continental crust

Previous structural studies revealed that the formation of south Karakoram domes are not controlled by any major detachment such as the south Tibetan or Pamir domes (e.g. Brunel et al., 1994; Lee et al., 2004, 2006; Thiede et al., 2006; Robinson et al., 2007; Langille et al., 2010). They are thus not related with any sig-

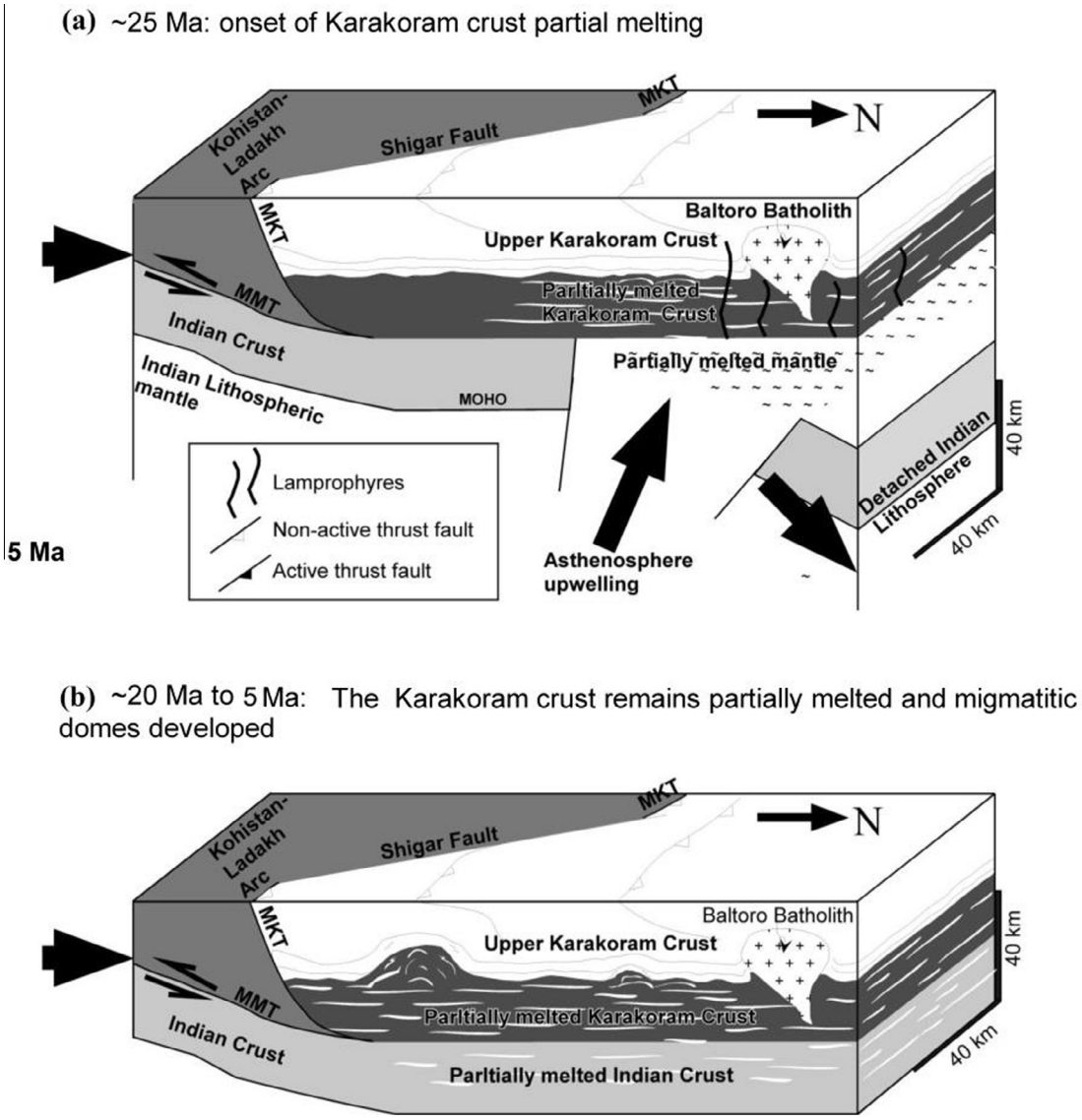

Fig. 11. Conceptual geodynamic model for the Miocene evolution of the south Karakoram crust. (a) At ~25 Ma, Onset of Karakoram crust partial melting favoured by heat advection from mantle (lamprophyre) and crustal (Baltoro granite) melts. (b) Before exhumation and final cooling at ~5 Ma the Karakoram lower and middle crust remains partially melted and migmatitic domes developed. High temperature is maintained due to crustal thickening promoted by Indian continental crust underplating following slab breakoff. MKT: Main Karakoram Thrust, MMT: Main Mantle Thrust.

nificant horizontal displacement of partially melted continental crust. This geochronological study evidences that the south Karakorum middle crust partially melted before 20 Ma and that final crystallization occurred at about 5–6 Ma. During that time interval the south Karakorum middle crust remained partially melted and most probably was only affected by vertical (diapiric?) motions (Fig. 11). This behavior is very different from channel flow model proposed for the south Tibetan middle crust (Beaumont et al., 2001) at around 20–10 Ma. Actually lack of significant horizontal displacement is more in accordance with numerical simulation of crustal behavior for a thickened orogenic plateau proposed by Rey et al. (2010) where diapiric motion are significant. Thus this study questions the existence of channel flow at least in the western India–Asia convergent zone.

7. Conclusion

- The inherited cores of zircons are Proterozoic (1.8–1.9 Ga) with some Paleoproterozoic ages (2.3–2.5 Ga). The 1.8–1.9 Ga ages have also been observed in south Tibet/Lhasa block and other parts of the world and are mainly attributed to the Transamazonian orogeny. The onset of partial melting in the Dassu dome took place between 22 and 20 Ma and lasted until 5–6 Ma at about 25–30 km depth (6–8 kbar) as evident by the crystallization ages of 20–5 Ma from rims around the Precambrian core and relationship with surrounding litho-tectonic units.
- Both the inherited cores and the Neogene overgrowths yielded indistinguishable homogeneous oxygen isotopic composition generally ranging from 7.5‰ to 9.5‰. This indicates that the (1) zircons crystallized from the evolved infracrustal sources with some contribution from supracrustal material and (2) that the Neogene overgrowth are the precipitated melt generated by partial melting of Precambrian crust. The homogeneous elevated oxygen composition is consistent with the absence of pristine mantle-derived magmas.
- The Hf isotopic composition of Neogene overgrowth is significantly less-evolved than the inherited core. This coupled with the lack of dissolution structure; involvement of any radiogenic external melts is likely. Therefore, contamination from less-evolved Neogene magmatism in the Baltoro region is proposed.

- Following partial melting, before 20 Ma, the middle crust remained partially melted until 5–6 Ma and was not affected by significant horizontal displacement as proposed for in south Tibet at similar time.

Acknowledgements

We are grateful to Dominique Giesler, Mark Pecha and Dr. Clayton Loehn at LaserChron, University of Arizona for technical assistance in the sample preparation, analysis, and data reduction isotopic data (U–Pb and Hf) acquisition and zircon BSE & CL-imaging. The authors also thank Dr. Kouki Kitajima at WiscSIMS, UW-Madison for tuning and operation of the IMS-1280 instrument and assistance with sample preparation, analysis (oxygen isotopic measurements), and data reduction and interpretation. WiscSIMS is partly supported by NSF-EAR1053466." We also thank Dr. Gail L Arnold for her comments and suggestions.

Appendix A. Supplementary material

Supplementary data associated with this article can be found, in the online version, at http://dx.doi.org/10.1016/j.jseaes.2016.01.014.

References

Allen, T., Chamberlain, P.C., 1991. Metamorphic evidence for an inverted crustal section, with constraints on the Main Karakoram thrust, Baltistan, northern Pakistan. J. Metamorph. Geol. 9, 403–418.

Beaumont, C., Jamieson, R.A., Nguyen, M.N., Lee, B., 2001. Himalayan tectonics explained by extrusion of a low-viscosity crustal channel coupled to focused surface denudation. Nature 414, 738–742.

Bertrand, J.M., Kienast, J.R., Pinardon, J.L., 1988. Structure and metamorphism of the Karakoram gneisses in the Braldu–Baltoro Valley (North Pakistan). Geodin. Acta 2, 135–150.

Bouvier, A., Vervoort, J.D., Patchett, J.D., 2008. The Lu-Hf and Sm-Nd isotopic composition of CHUR: Constraints from unequilibrated chondrites and implications for the bulk composition of terrestrial planets. Earth Planet. Sci. Lett. 273, 48–57.

Brunel, M., Arnaud, N., Tapponnier, P., Pan, Y., Wang, Y., 1994. Kongur Shan normal fault: type example of mountain building assisted by extension (Karakoram Fault, eastern Pamir). Geology 22, 707–710.

Butler, R.W.H., Casey, M., Lloyd, G.E., Bond, C.E., McDade, P., Shipton, Z., Jones, R., 2002. Vertical stretching and crustal thickening at Nanga Parbat, Pakistan Himalaya: a model for distributed continental deformation during mountain building. Tectonics 21, 9–1.

Butler, R.W.H., Prior, D.J., 1988. Tectonic controls on the uplift of the Nanga Parbat Massif, Pakistan Himalayas. Nature 333, 247–250.

Cavosie, A.J., Valley, J.W., Wilde, S.A., E.I.M.F., 2005. Magmatic $\delta^{18}O$ in 4400–3900 Ma detrital zircons: a record of the alteration and recycling of crust in the early Archean. Earth Planet. Sci. Lett. 235, 663–681.

Cecil, R., Gehrels, G., Patchett, J., Ducea, M., 2011. U–Pb–Hf characterization of the central Coast Mountains batholith: implications for petrogenesis and crustal architecture. Lithosphere 3, 247–260.

Corfu, F., Hanchar, J.M., Hoskin, P.W.O., Kinny, P., 2003. Atlas of zircon textures. In: Hanchar, J.M., Hoskin, P.W.O. (Eds.), Zircon. Mineralogical Society of America & Geochemical Society, Reviews in Mineralogy and Geochemistry.

Coward, M.P., Windley, B.F., Broughton, I.W., Luff, M.G., Petterson, M.G., Pudsey, C.J., Rex, D.C., Khan, M.A., 1986. Collision tectonics in the NW Himalayas. In: Coward, M.P., Ries, A.C. (Eds.), Collision Tectonics. Geological Society of London Special Publications 19, pp. 203–219.

Crowley, J.L., Waters, D.J., Searle, M.P., Bowring, S.A., 2009. Pleistocene melting and rapid exhumation of the Nanga Parbat massif, Pakistan: age and P-Tconditionsof accessory mineral growth in migmatite and leucogranite. Earth Planet. Sci. Lett. 3, 408–420.

Debon, F., Le Fort, P., Dautel, D., Sonet, J., Zimmermann, J.L., 1987. Granites of western Karakorum and northern Kohistan (Pakistan): a composite Mid-Cretaceous to upper Cenozoic magmatism. Lithos 20, 19–40.

Dong, X., Zhang, Z., Liu, F., Wang, W., Yu, F., Shen, K., 2011. Zircon U–Pb geochronology of the Nyainqentanglha Group from the Lhasa terrane: new constraints on the Triassic orogeny of the south Tibet. J. Asian Earth Sci. 42, 732–739.

Flowerdew, M.J., Millar, I.L., Vaughan, A.P.M., Horstwood, M.S.A., Fanning, C.M., 2006. The source of granitic gneisses and migmatites in the Antarctic Peninsula: a combined U–Pb SHRIMP and laser ablation Hf isotope study of complex zircons. Contrib. Miner. Petrol. 151, 751–768.

Fraser, J.E., Searle, M.P., Parrish, R.R., Noble, S.R., 2001. Chronology of deformation, metamorphism, and magmatism in the southern Karakoram Mountains. Geol. Soc. Am. Bull. 113, 1443–1455.

Gehrels, G., Pecha, M., 2014. Detrital zircon U–Pb geochronology and Hf isotope geochemistry of Paleozoic and Triassic passive margin strata of western North America. Geosphere 10, 49–65.

Gehrels, G., Rusmore, M., Woodsworth, G., Crawford, M., Andronicos, C., Hollister, L., Patchett, J., Ducea, M., Butler, R., Klepeis, K., Davidson, C., Mahoney, B., Friedman, R., Haggart, J., Crawford, W., Pearson, D., Girardi, J., 2009. U–Th–Pb geochronology of the Coast Mountains Batholith in north-coastal British Columbia: constraints on age, petrogenesis, and tectonic evolution. Geol. Soc. Am. Bull. 121 (9/10), 1341–1361.

Gehrels, G.E., Valencia, V.A., Ruiz, J., 2008. Enhanced precision, accuracy, efficiency, and spatial resolution of U–Pb ages by laser ablation-multicollector-inductively coupled plasma-mass spectrometry. Geochem. Geophys. Geosyst. 9, Q03017.

Guillot, S., Le Fort, P., 1995. Geochemical constraints on the bimodal origin of High Himalayan leucogranites. Lithos 35, 221–234.

Guo, Z., Wilson, M., 2011. The Himalayan leucogranites: constraints on the nature of their crustal source region and geodynamic setting. Gondwana Res. 22, 360–376.

Hanson, C.R., 1989. The northern suture in the Shigar valley, Baltistan, northern Pakistan. Geol. Soc. Am. Spec. Pap. 232, 203–215.

Harris, N., Massey, J., 1994. Decompression and anatexis of Himalayan metapelites. Tectonics 13, 1537–1546.

Hoskin, P.W.O., Black, L.P., 2000. Metamorphic zircon formation by solid state recrystallization of protolith igneous zircon. J. Metamorph. Geol. 18, 423–439.

Kelsey, D.E., Clark, C., Hand, M., 2008. Thermobarometric modelling of zircon and monazite growth in melt-bearing systems: examples using model metapelitic and metapsammitic granulites. J. Metamorph. Geol. 26, 199–212.

Kita, N.T., Ushikubo, T., Fu, B., Valley, J.W., 2009. High precision SIMS oxygen isotope analyses and the effect of sample topography. Chem. Geol. 264, 43–57.

Krol, M.A., Zeitler, P.K., Poupeau, G., Pêcher, A., 1996. Temporal variations in the cooling and denudation history of the Hunza plutonic complex, Karakoram Batholith, revealed by $^{40}Ar/^{39}Ar$ thermochronology. Tectonics 15, 403–415.

Langille, J., Lee, J., Hacker, B., Seward, G., 2010. Middle crustal ductile deformation patterns in southern Tibet: insights from vorticity studies in Mabja Dome. J. Struct. Geol. 32, 70–85.

Lee, J., McClelland, W., Wang, Y., Blythe, A., McWilliams, M., 2006. Oligocene–Miocene middle crustal flow in the southern Tibet: geochronology of Mabja Dome. In: Law, R.D., Searle, M.P., Godin, L. (Eds.), Channel Flow, Ductile Extrusion and Exhumation in Continental Collision Zones. Geological Society, London, Special Publication 268, pp. 445–469.

Lee, J., Hacker, B.R., Wang, Y., 2004. Evolution of the north Himalayan Gneiss Domes: structure and metamorphic studies in Mabja Dome, southern Tibet. J. Struct. Geol. 26, 2297–2316.

Le Fort, P., Tongiorgi, M., Gaetani, M., 1994. Discovery of a crystalline basement and Early Ordovician marine transgression in the Karakoram Mountain Range, Pakistan. Geology 22, 941–944.

Le Fort, P., Cuney, M., Deniel, C., France-Lanord, C., Sheppard, S.M.F., Upreti, B.N., Vidal, P., 1987. Crustal generation of the Himalayan leucogranites. Tectonophysics 134 (1–3), 39–57.

Le Fort, P., 1986. Metamorphism and Magmatism During the Himalayan Collision. In: Coward, M.P., Ries, A.C. (Eds.), Collision Tectonics. Special Publication, Geological Society of London 19, pp. 159–172.

Le Fort, P., Michard, A., Sonet, J., Zimmermann, J.L., 1983. Petrography, geochemistry and geochronology of some samples from the Karakoram axial batholith (Northern Pakistan). In: Shams, F.A. (Ed.), Granites of the Himalaya, Karakoram and Hindu Kush. Lahore University, Pakistan, pp. 377–387.

Lemennicier, Y., Le Fort, P., Lombardo, B., PeÃcher, A., Rolfo, F., 1996. Tectonometamorphic evolution of the central Karakorum (Baltistan ± northern Pakistan). Tectonophysics 260, 119–143.

Mahar, M.A., Mahéo, G., Goodell, P.C., Pavlis, T.L., 2014. Age and origin of post collision Baltoro granites, south Karakoram, North Pakistan: Insights from in-situ U–Pb, Hf and oxygen isotopic record of zircons. Lithos 205, 341–358.

Mahéo, G., Blichert-Toft, J., Pin, C., Guillot, S., Pêcher, A., 2009. Partial melting of mantle and crustal sources beneath South Karakorum, Pakistan: implications for the Miocene geodynamic evolution of the India–Asia convergence zone. J. Petrol. 50, 427–449.

Mahéo, G., Pêcher, A., Guillot, S., Rolland, Y., Delacourt, C., 2004. Exhumation of Neogene gneiss domes between oblique crustal boundary in South Karakorum (NW Himalaya, Pakistan). In: Whitney, D.L., Teyssier, V., Siddoway, C.S. (Eds.), Gneiss Domes in Orogeny. Geological Society of America, Special Papers 380, pp. 141–154.

Mahéo, G., Guillot, S., Blichert-Toft, J., Rolland, Y., Pêcher, A., 2002. A slab breakoff model for the Neogene thermal evolution of South Karakorum and South Tibet. Earth Planet. Sci. Lett. 195, 45–58.

Nelson, K.D., Zhao, Wenjin, Brown, L.D., Kuo, J., Che, Jinkai, Lui, Xianwen, Klemper, S. L., Makovsky, Y., Meissner, R., Mechie, J., Kind, R., Wenzel, F., Ni, J., Nabelek, J., Chen, Leshou, Tan, Handong, Wei, Wenbo, Jones, A.G., Booker, J., Unsworth, M., Kidd, W.S.F., Hauck, M., Alsdorf, D., Ross, A., Cogan, M., Changde, Wu, Sandvol, E., Edwards, M., 1996. Partially molten middle crust beneath southern Tibet: Synthesis of Project INDEPTH initial results. Science 274, 1684–1688.

Palin, R.M., Searle, M.P., Waters, D.J., Horstwood, M.S.A., Parrish, R.R., 2012. Combined thermobarometry and geochronology of peraluminous metapelites from the Karakoram metamorphic complex, North Pakistan; New insight into

the tectonothermal evolution of the Baltoro and Hunza Valley regions. J. Metamorph. Geol. 30, 793–820.
Parrish, R.R., Tirrul, R., 1989. U–Pb age of the Baltoro granite, northwest Himalaya, and implications for zircon inheritance and monazite U–Pb systematics. Geology 17, 1076–1079.
Pêcher, A., Seeber, L., Guillot, S., Jouanne, F., Kausar, A., Latif, M., Majid, A., Mahéo, G., Mugnier, J.L., Rolland, Y., Van der Beek, P., Van Melle, J., 2008. Stress field evolution in the northwest Himalayan syntaxis northern Pakistan. Tectonics 27, TC6005.
Pegler, G., Das, S., 1998. An enhanced image of the Pamir Hindu Kush seismic zone from relocated earthquake hypocentres. Geophys. J. Int. 134, 573–595.
Pognante, U., 1991. Shoshonitic and ultrapotassic postcollisional dykes from northern Karakoram (Sinkiang, China). Lithos 26, 305–316.
Rey, P.F., Teyssier, C., Kruckenberg, S.C., Whitney, D.L., 2011. Viscous collision in channel explains double domes in metamorphic core complexes. Geology 39, 387–390.
Rey, P.F., Teyssier, C., Whitney, D.L., 2010. Limit of channel flow in orogenic plateaux. Lithosphere 2, 328–332.
Rex, A.J., Searle, M.P., Tirrul, R., Crawford, M.B., Prior, D.J., Rex, D.C., Barnicoat, A., 1988. The geochemical and tectonic evolution of the Central Karakorum, North Pakistan. Philos. Trans. R. Soc. Lond. Ser. A 326, 229–255.
Rey, P.F., Teyssier, C., Whitney, D.L., 2009a. Extension rates, crustal melting, and core complex dynamics. Geology 37, 391–394.
Rey, P.F., Teyssier, C., Whitney, D.L., 2009b. The Role of Partial Melting and Extensional Strain Rates in the Development of Metamorphic Core Complexes. In: Chardon, D., Rey, P., Teyssier, C., Whitney, D.L. (Eds.), Hot Orogen: Tectonophysics 477, pp. 135–144.
Robinson, A.C., Yin, A., Manning, C.E., Harrison, T.M., Zhang, S.H., Wang, X.F., 2007. Cenozoic evolution of the eastern Pamir: implications for strain-accommodation mechanisms at the western end of the Himalayan–Tibetan orogen. Geol. Soc. Am. Bull. 119, 882–896.
Rolland, Y., Villa, I.M., Guillot, S., Mahéo, G., Pêcher, A., 2006. Evidence for Pre-Cretaceous history and partial Neogene (19–9 Ma) reequilibration in the Karakorum (NW Himalayan Syntaxis) from 40Ar–39Ar amphibole dating. J. Asian Earth Sci. 27, 371–391.
Rolland, Y., Carrio-Schaffhauser, E., Sheppard, S.M.F., Pêcher, A., Esclauze, L., 2005. Metamorphic zoning and geodynamic evolution of an inverted crustal section (Karakorum margin, N Pakistan), evidence for two metamorphic events. Int. J. Earth Sci. 95, 288–305.
Rolland, Y., Picard, C., Pecher, A., Carrio, E., Sheppard, S.M.F., Oddone, M., Villa, I.M., 2002. Presence and geodynamic significance of Cambro-Ordovician series of SE Karakoram (N Pakistan). Geodin. Acta 15, 1–21.
Rolland, Y., Mahéo, G., Guillot, S., Pêcher, A., 2001. Tectono-metamorphic evolution of the Karakorum Metamorphic Complex (Dassu-Askole area, NE Pakistan): exhumation of mid-crustal HT-MP gneisses in a convergent context. J. Metamorph. Geol. 19, 717–737.
Rubatto, D., Chakraborty, S., Dasgupta, S., 2013. Timescales of crustal melting in the Higher Himalayan Crystallines (Sikkim, Eastern Himalaya) inferred from trace element-constrained monazite and zircon chronology. Contrib Miner. Petrol. 165, 349–372.
Sawyer, E.W., 2008. Atlas of Migmatites. Mineralogical Association of Canada, Quebec; NRC Research Press, Ottawa The Canadian Mineralogist Special Publication 9.
Schärer, U., Copeland, P., Harrison, T.M., Searle, M.P., 1990. Age, cooling history and origin of postcollisional leucogranites in the Karakoram batholith, a multisystem isotope study. J. Geol. 98, 233–251.
Searle, M.P., Parrish, R.R., Thow, A.V., Noble, S., Phillips, R.J., Waters, D.J., 2010. Anatomy, age and evolution of a collisional mountain belt: the Baltoro granite batholith and Karakoram Metamorphic Complex, Pakistani Karakoram. J. Geol. Soc. 167, 183–202.
Searle, M.P., Tirrul, R., 1991. Structural and thermal evolution of the Karakoram crust. J. Geol. Soc. London 148, 65–82.
Searle, M.P., Rex, A.J., Tirrul, R., Rex, D.C., Barnicoat, A., Windley, B.F., 1989. Metamorphic, magmatic and tectonic evolution of the Central Karakoram in the Biafo–Baltoro–Hushe regions of northern Pakistan. Geol. Soc. Am. Spec. Pap. 232, 47–74.
Seong, Y.B., Owen, L.A., Bishop, M.P., Bush, A., Clendon, P., Copland, L., Finkel, R.C., Kamp, U., Shroder, J.F., 2008. Rates of fluvial bedrock incision within an actively uplifting orogen: Central Karakoram Mountains, northern Pakistan. Geomorphology 97, 274–286.
Shieh, Y.N., 1985. High $\delta^{18}O$ granitic plutons from the Frontenac Axis, Grenville Province of Ontario, Canada. Geochim. Cosmochim. Acta 49, 117–123.
Smith, H.A., 1993. Characterization and Timing of Metamorphism Within the Indo–Asian Suture Zone, Himalayas, Northern Pakistan, PhD thesis. Dartmouth College, Hanover, New Hampshire.
Tahirkheli, R.A.K., Jan, M.Q., 1979. Geology of Kohistan, Karakoram Himalaya. Univ. Peshawar Geol. Bull. 15, 1–30.
Teyssier, C., Whitney, D.L., 2002. Gneiss domes and orogeny. Geology 30, 1139–1142.
Thiede, R.C., Arrowsmith, J.R., Bookhagen, B., McWilliams, M., Sobel, E.R., Strecker, M.R., 2006. Dome formation and extension in the Tethyan Himalaya, Leo Pargil, northwest India. Geol. Soc. Am. Bull. 118, 635–650.
Thompson, A.B., Connolly, J.A.D., 1995. Melting of the continental crust; some thermal and petrological constraints on anatexis in continental collision zones and other tectonic settings. J. Geophys. Res. 100, 15565–15579.
Treloar, P.J., Rex, D.C., 1990. Cooling and uplift histories of the crystalline thrust stack of the Indian Plate internal zones west of Nanga Parbat, Pakistan Himalaya. Tectonophysics 180, 323–349.
Valley, J.W., Kita, N.T., 2009. In situ oxygen isotope geochemistry by ion microprobe. In: Fayek, M. (Ed.), MAC Short Course: Secondary Ion Mass Spectrometry in the Earth Sciences, 41. Mineralogical Association of Canada, Quebec, pp. 19–63.
Valley, J.W., Lackey, J.S., Cavosie, A.J., Clechenko, C.C., Spicuzzo, M.J., Basei, M.A.S., Bindeman, I.N., Ferreira, V.P., Sial, A.N., King, E.M., Peck, W.H., Sinha, A.K., Wei, C. S., 2005. 4.4 billion years of crustal maturation. Contrib. Miner. Petrol. 150, 561–580.
Valley, J.W., 2003. Oxygen isotopes in zircon. In: Hanchar, J.M., Hoskin, P.W.O. (Eds.), Zircon: Reviews in Mineralogy and Geochemistry 53, pp. 343–386.
Valley, J.W., Kinny, P.D., Schulze, D.J., Spicuzza, M.J., 1998. Zircon megacrysts from kimberlite: oxygen isotope variability among mantle melts. Contrib. Miner. Petrol. 133, 1–11.
Visona, D., Lombardo, B., 2002. Two-mica and tourmaline leucogranites from the Everest-Makalu region (Nepal-Tibet). Himalayan leucogranite genesis by isobaric heating? Lithos 62, 125–150.
Zanchi, A., Gaetani, M., 1994. Introduction to the geological map of the North Karakorum terrane from the Chapursan Valley to the Shimshal Pass 1:150,000 scale. Riv. Ital. Paleontol. Stratigr. 100, 125–135.
Zeitler, P.K., Koons, P.O., Bishop, M.P., Chamberlain, C.P., Craw, D., Edwards, M.A., Hamidullah, S., Jan, M.Q., Khan, M.A., Khattak, M.U.K., Kidd, W.S.F., Mackie, R.L., Meltzer, A.S., Park, S.K., Pecher, A., Poage, M.A., Sarker, G., Schneider, D.A., Seeber, L., Shroder, J.F., 2001. Crustal reworking at Nanga Parbat, Pakistan: Metamorphic consequences of thermal-mechanical coupling facilitated by erosion. Tectonics 20, 712–728.
Zeitler, P.K., 1985. Cooling history of the NW Himalaya, Pakistan. Tectonics 4, 127–151.
Zhao, G.C., Cawood, P.A., Wilde, S.A., Sun, M., 2002. Review of global 2.1–1.8 Ga orogens: implications for a pre-Rodinia supercontinent. Earth Sci. Rev. 59, 125–162.
Zhu, D.C., Zhao, Z.D., Niu, Y.L., Dilek, Y., Hou, Z.Q., Mo, X.X., 2013. The origin and pre-Cenozoic evolution of the Tibetan Plateau. Gondwana Res. 23, 1429–1454.
Zhu, D.C., Mo, X.X., Niu, Y.L., Zhao, Z.D., Wang, L.Q., Pan, G.T., Wu, F.Y., 2009. Zircon U–Pb dating and in-situ Hf isotopic analysis of Permian peraluminous granite in the Lhasa terrane, southern Tibet: implications for Permian collisional orogeny and paleogeography. Tectonophysics 469, 48–60.